Available online at www.sciencedirect.com
ScienceDirect
Icarus 190 (2007) 110–126
ICARUS
www.elsevier.com/locate/icarus

The effects of vigorous mixing in a convective model of zonal flow on the ice giants

Jonathan Aurnou [a,*], Moritz Heimpel [b], Johannes Wicht [c]

[a] *Earth and Space Sciences, UCLA, 5690 Geology Bldg., Los Angeles, CA 90095-1567, USA*
[b] *Department of Physics, University of Alberta, Edmonton, Alberta, T6G 2J1, Canada*
[c] *Max Planck Institute for Solar System Research, 37191 Katlenburg-Lindau, Germany*

Received 23 March 2006; revised 22 January 2007

Available online 18 April 2007

Abstract

Previous studies have used models of three-dimensional (3D) Boussinesq convection in a rotating spherical shell to explain the zonal flows on the gas giants, Jupiter and Saturn. In this paper we demonstrate that this approach can also generate flow patterns similar to those observed on the ice giants, Uranus and Neptune. The equatorial jets of Uranus and Neptune are often assumed to result from baroclinic cloud layer processes and have been simulated with shallow layer models. Here we show that vigorous, 3D convection in a spherical shell can produce the retrograde (westward) equatorial flows that occur on the ice giants as well as the prograde (eastward) equatorial flows of the gas giants. In our models, the direction of the equatorial jet depends on the ratio of buoyancy to Coriolis forces in the system. In cases where Coriolis forces dominate buoyancy, cylindrical Reynolds stresses drive prograde equatorial jets. However, as buoyancy forces approach and exceed Coriolis forces, the cylindrical nature of the flow is lost and 3D mixing homogenizes the fluid's angular momentum; the equatorial jet reverses direction, while strong prograde jets form in the polar regions. Although the results suggest that conditions involving strong atmospheric mixing are responsible for generating the zonal flows on the ice giants, our present models require roughly 100 and 10 times the internal heat fluxes observed on Uranus and Neptune, respectively.

Keywords: Uranus; Neptune; Atmospheres, dynamics; Interiors

1. Introduction

The surface winds on the giant planets, Jupiter, Saturn, Uranus and Neptune, are determined by tracking cloud features in the outer weather layers. The observations, mainly derived from Voyager, Galileo and Cassini mission imaging as well as from Hubble Space Telescope and ground-based telescope observations (Porco et al., 2003, 2005; Perez-Hoyos et al., 2005; Vasavada and Showman, 2005), show that zonally-directed (east–west) motions dominate the surface flow fields. On each of these planets, these zonal winds form complex, distinct jet patterns that alternate between the prograde (eastward) and retrograde (westward) flow direction. The zonal wind velocities are measured relative to the planet's mean rotational motion, which is assumed to correspond with the reference frame of the deep-seated planetary magnetic field (e.g., Russell et al., 2001).

The zonal winds on Jupiter and Saturn feature prograde jets in the equatorial region (Fig. 1a). Their equatorial jets are flanked at higher latitudes by multiple smaller-scale zonal jet structures. Jupiter's prograde equatorial jet extends in latitude over roughly $\pm 20°$ and reaches a peak velocity of approximately $+150$ m/s. To the north of the equatorial jet lies another strongly prograde jet, while to the south lies a retrograde jet. At higher latitudes, approximately ten smaller amplitude, relatively narrow, alternating jets dominate the flow field in each hemisphere (Porco et al., 2003). The powerful prograde equatorial jet on Saturn is broader than Jupiter's, extending from about $\pm 35°$ latitude and reaching a peak velocity of nearly $+450$ m/s (Porco et al., 2005). At higher latitudes on Saturn, only three prograde jets are found in each hemisphere. Curiously, there is

* Corresponding author. Fax: +1 310 825 2779.
E-mail address: aurnou@ucla.edu (J. Aurnou).

0019-1035/$ – see front matter
doi:10.1016/j.icarus.2007.02.024

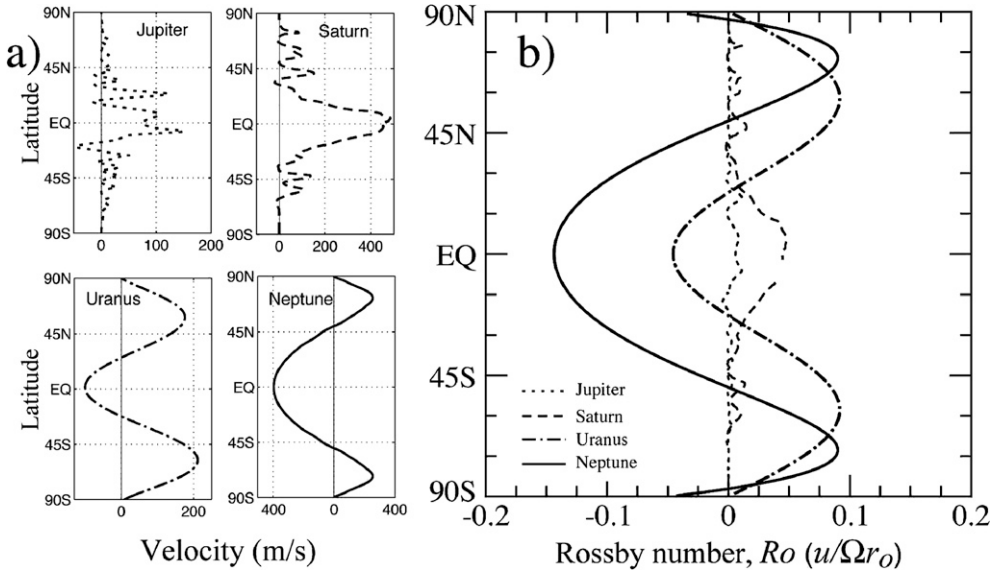

Fig. 1. Observed surface zonal (i.e., azimuthal) velocity profiles on the gas giants: Jupiter (short-dashed lines); Saturn (long-dashed); Uranus (dot-dashed); Neptune (solid). (a) Zonal wind velocities given in m/s. Profiles adapted from Sukoriansky et al. (2002). (b) Zonal wind velocities given in Rossby number units, $Ro = u/\Omega r_O$. Profiles adapted from Porco et al. (2003), Sanchez-Lavega et al. (2000), Hammel et al. (2001) and Sromovsky et al. (1993).

almost no retrograde surface zonal flow relative to the Saturn's magnetic field reference frame.

On Uranus and Neptune, the equatorial jets are retrograde, opposite those of Jupiter and Saturn. In further contrast, the higher latitudes of Uranus and Neptune do not contain multiple jets. Instead, the retrograde equatorial jet is flanked by one strong high-latitude prograde jet in each hemisphere (Fig. 1a). Although the cloud deck on Uranus shows little observable contrast, Hubble and Keck imaging data appear to show that its retrograde equatorial jet has a peak velocity of roughly $+100$ m/s and extends between $\sim\pm 30°$ latitude (Hammel et al., 2001; 2005). At higher latitudes, the strongly prograde flow reaches maximum velocities that exceed $+200$ m/s. On Neptune, an even broader, more powerful retrograde jet extends over $\sim\pm 50°$ latitude. The peak equatorial flow velocity is close to -400 m/s. At higher latitudes, strong prograde jets are estimated to reach peak velocities of nearly $+250$ m/s (Sromovsky et al., 2001; Fry and Sromovsky, 2004).

In addition to observations of large-scale zonal flows, measurements of outward heat flux have also been made for the jovian planets (Ingersol, 1990). On Jupiter, Saturn and Neptune, the measured thermal emissions are greater than the insolation received (Vasavada and Showman, 2005). The ratio of total outward thermal emission and insolation, q^*, is roughly 1.7 for Jupiter. On Saturn, q^* is close to 1.8, while for Neptune $q^* \sim 2.6$ (Lodders and Fegley, 1998). For q^* to take on values greater than unity, an outward flux of thermal energy must be escaping the planet's interior that is comparable to or greater than the external solar energy deposition. Ingersoll and Pollard (1982) have shown that such a deep flux of interior heat is capable of driving deep convective motions within the molecular atmospheric layers of the jovian planets.

Uranus is the exception with $q^* \lesssim 1.14$ (Lodders and Fegley, 1998). The qualitative difference in heat flow between Uranus and Neptune may be caused by a compositionally-stable interior layer in Uranus that impedes convection and limits the outward flux of heat from the deep interior (Podolak et al., 1991). Such a compositional layer, should it exist, must be relatively small in radial extent as it cannot be detected in interior models that fit the planet's observed gravitational moments (Hubbard et al., 1991, 1995; Zhang, 1997). In addition to similar patterns of surface zonal flow, Uranus and Neptune also have similar planetary magnetic field morphology, with strong nonaxial quadrupole and octupole components (e.g., Holme, 1997). It remains to be explained why Uranus and Neptune, with their similar internal structures (Hubbard et al., 1991; Zhang, 1997) but strongly differing outward heat flows, generate comparable surface zonal winds and planetary magnetic fields (e.g., Beebe, 2005).

Observations and theoretical models suggest that surface zonal flows observed on the jovian planets can extend below the observable surface layers (Ingersoll and Pollard, 1982; Atkinson et al., 1998; Showman et al., 2006). The depth at which such deep zonal flows are truncated is strongly affected by the interior structure of each particular planet. The outermost fluid layers of Jupiter and Saturn undergo a phase transition with depth from molecular to metallic hydrogen. This liquid metal interior is thought to be the generation region of the jovian planets' magnetic fields. The metalization transition has been estimated to occur at 0.80–0.85 of Jupiter's radius (Guillot et al., 2004). On Saturn, this pressure dependent transition occurs at greater depth, 0.6–0.8 of its radius, due to its smaller mass (Hubbard and Stevenson, 1984).

The attenuation of zonal flows with depth can result from the effects of increasing density within the planet (Evonuk and Glatzmaier, 2004). In addition, electromagnetic induction effects can become important in regions where the electrical conductivity is nonzero (Kirk and Stevenson, 1987). Zonal flows in electrically conductive fluids can act to shear out the ambient planetary magnetic field. The resulting Lorentz forces

will act against these shearing motions and will tend to damp the zonal velocities, as seen in numerical dynamo simulations (Christensen et al., 1999; Busse, 2002). The precise depth at which magnetic damping becomes significant on each of these planets is not presently known. However, it has been estimated to occur at between 0.85–0.95 of Jupiter's radius and between 0.6 and 0.8 of Saturn's radius (Kirk and Stevenson, 1987; Nellis et al., 1996; Guillot et al., 2004).

Uranus and Neptune's outer layers are comprised of hydrogen and helium with roughly solar compositions. This outermost layer transitions into the so-called "ice layer" at a depth of about 0.8 of Uranus' radius and 0.85 of Neptune's radius (Guillot, 1999). The layer is comprised of a mixture of H_2O, CH_4 and NH_3 and behaves like water at high pressure and temperature (Hubbard et al., 1991). However, this fluid is expected to be electrically-conductive due to molecular dissociation. Because interior pressures do not become great enough to metallize hydrogen (Nellis et al., 1996), deep-seated convection within the ice layer is likely to drive the dynamos on Uranus and Neptune (Ruzmaikin and Starchenko, 1991; Holme, 1997; Aubert and Wicht, 2004; Stanley and Bloxham, 2004).

The atmosphere–ice phase boundary, corresponding to a jump in density and conductivity, is likely to represent the maximum possible depth of significant zonal flow on the ice giants. Models by Hubbard et al. (1991), based on fitting the observed J_2 and J_4 gravitational moments, have shown that the surface zonal flows on Uranus and Neptune cannot extend globally on cylinders to great depths into their interiors, as first proposed for Jupiter by Busse (1976). However, Suomi et al. (1991) argue that deep convective motions in Neptune's equatorial region are thermodynamically possible and extend into the planet's interior, most likely down to depths of ∼2000–3000 km below the 1 bar pressure level, corresponding to 0.88–0.92 of Neptune's radius. Note that Soumi et al.'s (1991) estimates do not contradict Hubbard et al. (1991), because convection in a 2000–3000 km deep equatorial region is not likely to produce strong J_2 and J_4 perturbations. Suomi et al. (1991) state that deep convection can also occur on Uranus, but in a shallower fluid layer than on Neptune.

Fig. 1b shows the zonal flow profiles for the jovian planets given in terms of the Rossby number, *Ro*. This nondimensional number estimates the ratio between inertia forces in the fluid and Coriolis forces due to planetary rotation:

$$Ro = \frac{\text{inertia}}{\text{Coriolis}} \sim \frac{u^2/r_o}{\Omega u} = \frac{u}{\Omega r_o}, \tag{1}$$

where u is the zonal flow velocity measured with respect to the rotating frame of the planet, Ω is the planet's angular rotation velocity and the characteristic scale length is taken to be the planetary radius r_o. For Rossby numbers much less than 1, the fluid dynamics are expected to be dominated by planetary rotational effects; at *Ro* values approaching unity, inertial effects will become important. The peak Rossby numbers on Jupiter and Saturn are ∼ +0.012 and ∼ +0.045, respectively. The peak *Ro* value for Uranus is near to +0.08, whereas on Neptune this value is close to −0.15. Although the absolute *Ro* values for the jovian planets are less than unity, the ice giants' higher *Ro*-values and different zonal flow patterns suggest that they may operate in the dynamical regime where inertial forces strongly affect the zonal flows.

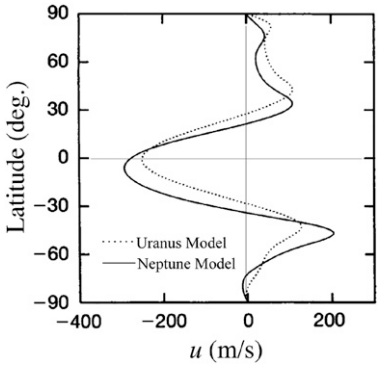

Fig. 2. Azimuthally-averaged zonal velocity profiles from the Uranus (dashed line) and Neptune (solid line) shallow layer models of Cho and Polvani (1996).

Previous studies of the zonal flow dynamics on the jovian planets have been of two predominant types: deep convection models and shallow layer models. For a recent review of zonal flow modeling, see Vasavada and Showman (2005). In the shallow layer models, turbulent fluid motions are restricted to the two horizontal dimensions on the spherical outer surface (e.g., Peltier and Stuhne, 2002; Williams, 2003). Due to the strong Coriolis forces in these models, the turbulence at mid- to high-latitudes freely evolves into alternating jets on the Rhines scale (Rhines, 1975; Yano et al., 2005). The equatorial jets in shallow layer models are almost always retrograde—in the correct direction to describe the equatorial jets on Uranus and Neptune. Due to this agreement with the observations of equatorial jet direction, it has been argued that rapidly-rotating, shallow layer turbulence, fueled by solar energy deposition, drives the ice giants' zonal winds (Cho and Polvani, 1996; Yano et al., 2005).

Fig. 2 shows the results of two shallow layer models from the work of Cho and Polvani (1996). The azimuthally-averaged surface zonal flow profile after 300 calculated planetary rotations is shown as a dashed line for the model of Uranus and as a solid line for the model of Neptune. Both models generate strong retrograde flows in the equatorial region, similar to the ice giants. These retrograde jets are flanked by high-latitude prograde flow structures that undulate in amplitude as a function of latitudinal position. Some of the shallow layer models equilibrate with large, coherent vortices in each hemisphere (Cho and Polvani, 1996; Cho et al., 2003). These large scale vortices can produce zonal flow profiles that are markedly asymmetric across the equatorial plane, as occurs for the Neptune case shown in Fig. 2.

In deep layer models, rapid rotation causes 3D convection to become nearly two-dimensional (2D) along the direction of the rotation axis. This type of flow is called quasi-geostrophic. Busse (1976) first argued that Jupiter's zonal winds could be driven by deep atmospheric convection. He suggested that the banded surface flow is an expression of deep quasi-geostrophic convection occurring on nested sets of convection

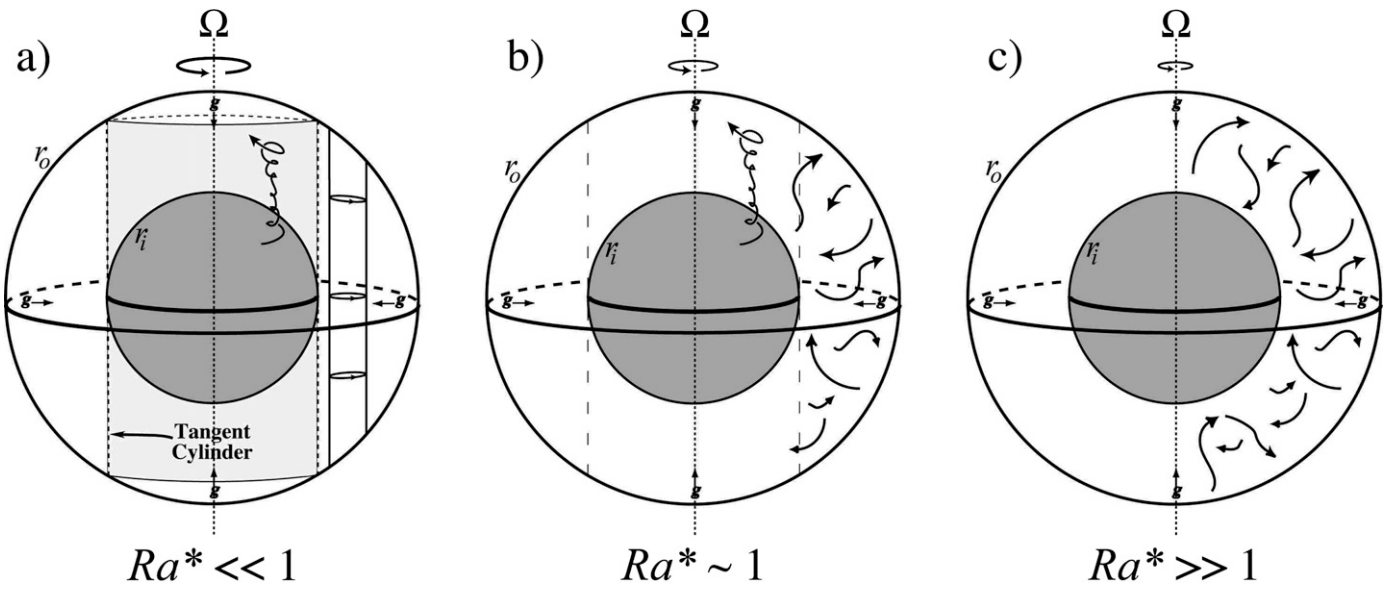

Fig. 3. Schematics showing different flow regimes from the thermal convection models in this study. To highlight the convective motions, these represent the flow field with the azimuthal flow component subtracted out. The spherical shell rotates at angular velocity Ω. The outer boundary is r_o; the inner boundary is r_i. The spherical shell radius ratio used in the simulations is $\chi = r_i/r_o = 0.75$. (For purposes of illustration $\chi = 0.50$ in this figure.) (a) The rapidly rotating case in which Coriolis forces dominate over buoyancy forces. (b) The transitional case in which the Coriolis and buoyancy forces are roughly comparable. (c) The slowly rotating case in which buoyancy forces dominate over Coriolis forces.

columns in the region outside of the axially-aligned "tangent cylinder," which is the imaginary, right cylinder that circumscribes the inner boundary equator (see Fig. 3a). Numerical models of rapidly rotating Boussinesq deep convection tend to produce prograde equatorial jets in the region outside the tangent cylinder, similar to those observed on Jupiter and Saturn (Aurnou and Olson, 2001; Christensen, 2001, 2002; Aurnou and Heimpel, 2004). In addition, recent deep convection models, that feature fully-developed quasigeostrophic turbulence in a relatively thin spherical shell geometry, develop higher latitude, Rhines scale alternating jets (Heimpel et al., 2005; Heimpel and Aurnou, 2007). Those models simultaneously generate realistic Jupiter-like zonal flows at both high and low latitudes.

In this paper we show that the mixing generated by vigorous, 3D convection can produce zonal wind patterns similar to those observed on Uranus and Neptune. In particular, we find that as planetary rotational forces are decreased, inertial effects come to dominate the dynamics and, consequently, strong convective mixing generates a zonal flow pattern with retrograde equatorial flow flanked by prograde jets at high latitudes. In Section 2, we present the governing equations and numerical model for thermal convection in a rapidly rotating spherical shell. Theoretical models of zonal flow generation are discussed in Section 3. In Section 4, we present the results of our calculations. Lastly, in Section 5 we show that convective mixing leads to angular momentum homogenization, which accounts for the zonal flows in our models. Further, we show that our convection models compare well with the zonal flow patterns on the ice giants even though they differ in their outward heat fluxes.

2. Governing equations and numerical methods

2.1. Governing equations

The equations governing rotating thermal convection in a spherical shell of Boussinesq fluid are the following.

$$\frac{\partial \mathbf{u}}{\partial t} + \mathbf{u}\cdot\nabla\mathbf{u} + 2\hat{z}\times\mathbf{u} = -\nabla p + Ra^* T(\mathbf{r}/r_o) + E\nabla^2\mathbf{u}, \quad (2)$$

$$\frac{\partial T}{\partial t} + \mathbf{u}\cdot\nabla T = EPr^{-1}\nabla^2 T, \quad (3)$$

$$\nabla\cdot\mathbf{u} = 0, \quad (4)$$

where $\mathbf{u}$ is the velocity vector, T is the temperature and p is the pressure. We nondimensionalize the system of equations using the spherical shell thickness $D = r_o - r_i$ for length scale, the inverse angular velocity Ω^{-1} for time scale, ΩD for velocity scale, $\rho\Omega^2 D^2$ for pressure scale and ΔT for temperature scale. Here ρ is the density of the Boussinesq fluid (e.g., Tritton, 1987). This means that the fluid in our model is incompressible except due to the effects of thermal perturbations. We consider the omission of compressibility effects to be the most severe

Table 1
Properties of the jovian planets

Planet	Equatorial radius [km]	Thermal emission, q^*	Rotation period [h]	Peak velocity [m/s]	Peak Rossby, Ro
Jupiter	7.2×10^4	1.7	9.9	+150	+0.012
Saturn	6.0×10^4	1.8	10.2	+450	+0.045
Uranus	2.6×10^4	$\lesssim$1.14	17.24	+215	+0.082
Neptune	2.5×10^4	$\sim$2.6	16.11	−400	−0.15

The thermal emission values given here are normalized by insolation. The Rossby numbers, Ro, are based upon the approximate peak surface zonal flow velocities.

Table 2
Nondimensional control parameters in Boussinesq rotating spherical shell convection

Parameter	Definition	Models	Ice giants	Giant planets
Radius ratio	$\chi = r_i/r_o$	0.75	∼0.80–1	∼0.80–1
Prandtl	$Pr = \nu/\kappa$	0.1–1	∼0.1	∼0.1
Ekman	$E = \nu/\Omega D^2$	3×10^{-4}–10^{-5}	$\sim 10^{-15}$	$\sim 10^{-18}$
Modified Rayleigh	$Ra^* = \alpha g_o \Delta T/\Omega^2 D$	10^{-2}–10^{1}	∼1?	∼0.01?

limitation of our present models, since the density scale height on the ice giants is estimated to be $H_\rho \sim 500$ km at mid-shell in our models (e.g., see Model N1 from Hubbard et al., 1991). Further following the Boussinesq approximation, the thermal expansion coefficient α, the kinematic viscosity ν, and the thermal diffusivity κ are all have constant values.

The nondimensional parameters that describe this system are given in Table 2 and depend on the fluid's kinematic viscosity ν, thermal diffusivity κ, thermal expansivity α and gravity given on the outer boundary, g_o. The Prandtl number Pr, which describes the physical properties of the fluid, is the ratio of the fluid's viscous and thermal diffusivities. The Ekman number E is the ratio of viscous and Coriolis forces. The modified Rayleigh number Ra^* is the nondimensionalized buoyancy forcing. The modified Rayleigh number can be re-written in terms of the standard Rayleigh number, $Ra = \alpha g_o \Delta T D^3/\nu\kappa$, as

$$Ra^* = \frac{Ra E^2}{Pr} = \frac{\alpha g_o \Delta T}{\Omega^2 D} \tag{5}$$

(Gilman, 1977; Christensen, 2002). The spherical shell geometry is defined by the radius ratio χ, which is the ratio of the bounding shell radii (see Fig. 3). For all the simulations performed in this study, we use $\chi = 0.75$ (i.e., $D/r_o = 1 - \chi = 0.25$), which corresponds to a ∼6000 km deep convection layer on the ice giants. Although we investigate convection in substantially deeper fluid layers than are estimated on the ice giants (Suomi et al., 1991; Guillot, 1999), the $\chi = 0.75$ spherical shell geometry is still relatively thin and allows us to use a far smaller numerical grid than in the comparable $\chi = 0.90$ simulations of Heimpel et al. (2005). In our models, the tangent cylinder intersects the outer boundary at $\cos^{-1}\chi = \pm 41^\circ$ latitude. We refer to the fluid outside the tangent cylinder as being in the spherical shell's equatorial region.

2.2. Numerical methods and techniques

In this study we carry out numerical simulations of Boussinesq thermal convection in rotating spherical shells. A detailed description of the numerical model, MagIC, is given by Wicht (2002). Equations (1)–(3) are solved simultaneously to determine the velocity and temperature fields, $\mathbf{u}$ and T. The calculations are performed subject to a constant temperature difference, ΔT, across the fluid layer. The thermal boundary conditions are isothermal. The mechanical boundary condition on the outer boundary r_o is mechanically free-slip; the inner boundary is either free-slip or rigid. The system's angular momentum is conserved to better than 0.01% in cases with free-slip inner and outer boundaries (Heimpel et al., 2005). Each case is initialized with zero flow relative to the rotating reference frame, i.e., in rigid body rotation. Convection develops from a randomly perturbed initial temperature field.

The pseudo-spectral numerical model, first developed by Glatzmaier (1984), uses mixed implicit/explicit time stepping and has been benchmarked in two independent studies (Christensen et al., 2001; Wicht, 2002). To save computational resources, we solve the governing equations on four-fold azimuthally-truncated spheres with periodic boundary conditions on the bounding meridian planes. It has been shown that azimuthal truncation does not strongly affect rotating convection solutions in spherical shells that are geometrically thin such that $\chi \gtrsim 0.70$ (Al-Shamali et al., 2004). Furthermore, we found little change in the resulting zonal flow field in a test case with 2-fold truncation.

In most of the simulations presented here, the outer boundary is free-slip and the inner boundary is rigid. These "mixed" mechanical boundary conditions have been used by Aurnou and Heimpel (2004) to study the effects of strong basal coupling in $Ra^* \ll 1$ models of jovian and saturnian zonal flows. They found that the zonal flows in the mixed cases are shifted such that the zonal velocity is close to zero along the tangent cylinder. In contrast, cases in which both boundaries are free-slip develop retrograde flows along the tangent cylinder in order to conserve angular momentum. Fig. 4 compares flow fields for free-slip and mixed boundary condition cases with $Ra^* = 0.09$, $E = 3 \times 10^{-4}$ and $Pr = 1$. Figs. 4a and 4b show zonal flow profiles on the outer surface and in the equatorial plane, respectively. Fig. 4c shows snapshots of the azimuthally-averaged temperature contours in the equatorial plane (left) and azimuthal velocity in a meridional plane (right). Note that the free-slip and the mixed cases have quite similar zonal flow and temperature structure in the equatorial region.

Although the equatorial flows in Fig. 4 are nearly the same (excepting the shift in relative velocity), the equilibration time in mixed cases can be an order of magnitude shorter than in cases in which both boundaries are free-slip. For this reason, we have chosen to employ mixed boundaries conditions in calculations made to determine the direction of the equatorial zonal flow over the range $10^{-2} < Ra^* < 10$. All the mixed cases have been run for at least $t = 0.5$ viscous diffusion times, D^2/ν. This corresponds to $t/(2\pi E) = 265$ planetary rotations at $E = 3 \times 10^{-4}$. However, the majority of the mixed cases were run for 1–3 viscous diffusion times, corresponding to roughly 500–1500 planetary rotations at $E = 3 \times 10^{-4}$. These cases are computed on a four-fold azimuthally truncated grid that has 81 radial levels, 576 points in latitude and 288 points in truncated azimuth. The maximum spherical harmonic degree calculated is $l_{\max} = 192$. The Prandtl number is fixed at $Pr = 1$. The majority of the mixed cases are made with $E = 3 \times 10^{-4}$, al-

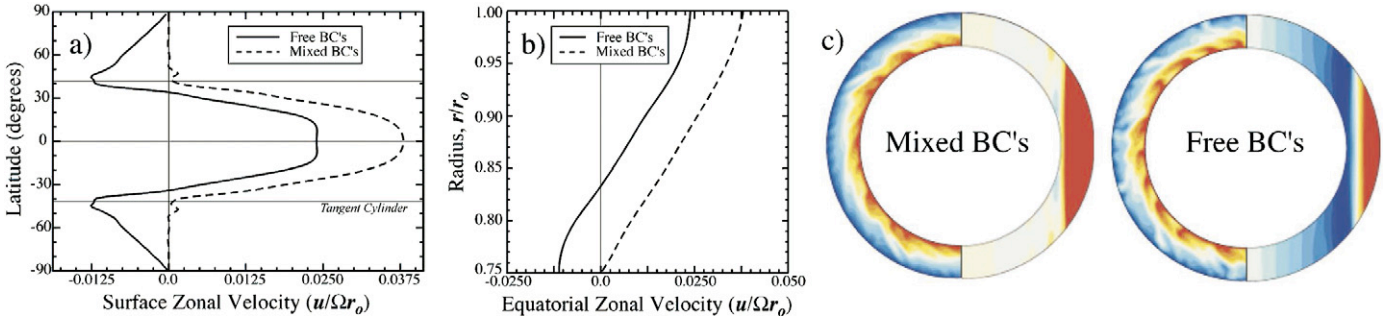

Fig. 4. Comparison between $Ra = 10^6$, $E = 3 \times 10^{-4}$, $Pr = 1$ cases with free-slip (solid lines) and mixed mechanical boundary conditions (dashed lines). (a) Latitudinal profiles of surface zonal flow Ro. (b) Radial profiles of zonal azimuthal velocity in the equatorial plane. (c) Color panels showing equatorial temperature contours viewed from above (left side) and azimuthally-averaged azimuthal velocity in a meridional plane (right side). In this figure red (blue) is positive (negative). Note that the two solutions are nearly identical, excepting the lack of retrograde flow in the mixed case.

though two cases are also presented at $E = 10^{-3}$ and $E = 10^{-4}$. No hyperdiffusivities are employed in the mixed calculations.

We have also carried out a case in which both boundaries are mechanically free-slip. This case generates a zonal flow pattern best approximating that of the ice giants. In addition to its free-slip boundaries, this case makes use of more extreme parameter values, closer to the asymptotic values relevant to planetary conditions. The parameter values for this case are $Ra = 1.5 \times 10^9$, $E = 10^{-5}$, $Pr = 0.1$ and $\chi = 0.75$, corresponding to a modified Rayleigh number of $Ra^* = 1.5$. The numerical grid for this case has eight-fold azimuthal truncation with 81 points in radius, 384 points in latitude and 128 points in azimuth. A moderate hyperdiffusivity is employed in this case, identical to that of Heimpel et al. (2005) and Heimpel and Aurnou (2007).

3. Regimes of deep convective zonal flow generation

Gilman (1977, 1978) first showed, via numerical simulations of the solar convection zone, that the mechanism of zonal flow generation qualitatively changes based on the ratio of buoyancy and Coriolis forces. This ratio is given as

$$\frac{\text{buoyancy force}}{\text{Coriolis force}} \sim \frac{\rho \alpha g_o \Delta T}{2\rho \Omega u} \sim \frac{\alpha g_o \Delta T}{\Omega u}. \tag{6}$$

Setting the characteristic velocity scale equal to the convective free-fall velocity across the fluid layer, $\vec{u}_{\text{conv}} \cdot \nabla \vec{u}_{\text{conv}} \sim \alpha \vec{g}_o \Delta T$ yields $u_{\text{conv}} \sim \sqrt{\alpha g_o \Delta T D}$, which leads to

$$\frac{\text{buoyancy force}}{\text{Coriolis force}} \sim \frac{\alpha g_o \Delta T}{\Omega \sqrt{\alpha g_o \Delta T D}} = \left(\frac{\alpha g_o \Delta T}{\Omega^2 D} \right)^{1/2} = \left(Ra^* \right)^{1/2}. \tag{7}$$

For cases in which $Ra^* \ll 1$, the Coriolis forces dominate the buoyancy forces that drive the convection, while buoyancy dominates over Coriolis in $Ra^* \gg 1$ cases. Because the convective free-fall velocity is estimated by balancing inertia and buoyancy forces, $(Ra^*)^{1/2}$ is also referred to as the convective Rossby number (e.g., Liu and Ecke, 1997; Miesch et al., 2000).

3.1. The rotation-dominated regime

Zonal flows in Boussinesq spherical shell convection are driven by two mechanisms: (1) Reynolds stresses produced by correlations of velocity components; (2) Coriolis forces acting on mean meridional circulation (Tilgner and Busse, 1997). Axially-aligned Reynolds stresses are the primary mechanism for generating zonal flows in $Ra^* \ll 1$ rotation-dominated cases, in which the Coriolis force tends to be balanced by pressure forces. Flows that satisfy this force balance are called geostrophic. Such flows are nearly invariant along the direction of the rotation axis, in accordance with the Taylor–Proudman theorem (Tritton, 1987), as shown schematically in Fig. 3a. In addition, these flows tend to conserve potential vorticity, $PV = (\zeta + 2\Omega)/h$ where $\zeta = \hat{z} \cdot \nabla \times \mathbf{u}$ is the axial vorticity and h is the axial height of the fluid column. In these quasi-2D flows, fluid moving cylindrically outward from the rotation axis is not deflected by the Coriolis force because it is counterbalanced by the induced pressure forces. Outside the tangent cylinder, the height of axial fluid columns decreases with cylindrical radius. This causes outward moving convection columns to become tilted in the prograde azimuthal direction in order to conserve potential vorticity (Zhang, 1992; Busse, 2002). The systematic prograde tilt of the axial columns generates Reynolds stresses: fluid traveling cylindrically outward from the rotation axis is correlated with prograde azimuthal flow; fluid traveling inward towards the rotation axis is correlated with retrograde azimuthal flow (see the equatorial temperature contours in Fig. 4c as well as the schematic in Fig. 5).

Should there be a displacement between constant pressure surfaces and constant density surfaces, then axially varying zonal flows, called thermal winds, will also develop in low Ra^* convection (Aurnou et al., 2003). However, in a convecting planetary atmosphere the fluid is likely to be isentropic and strong thermal winds are not likely to develop (Vasavada and Showman, 2005). Therefore, the first order terms in the governing equation for the quasigeostrophic zonal flow, $U(s,t)$, are (Zhang, 1992):

$$\frac{\partial U}{\partial t} = -\frac{\partial \langle u_\phi u_s \rangle}{\partial s} + \nu \frac{\partial^2 U}{\partial s^2}, \tag{8}$$

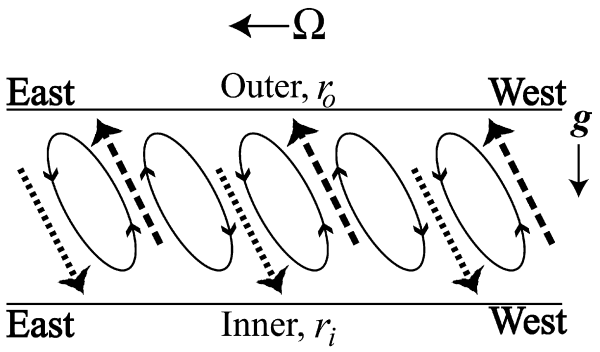

Fig. 5. Schematic showing azimuthally-tilted convection columns in low Ra^* convection, viewed from above. Cylindrically outward flows (long-dashed arrows) transport fluid with an prograde (eastward) azimuthal component of motion. Cylindrically inward flows (short-dashed arrows) transport fluid with a retrograde (westward) azimuthal component of motion. This produces angular momentum fluxes that drive a prograde jet by the outer boundary and a retrograde jet adjacent to the tangent cylinder.

where ϕ is azimuth and s is cylindrical radius. The first term on the right-hand side is the Reynolds stress term and the second term on the right-hand side represents the viscous force acting on the large-scale zonal flow. Outside the tangent cylinder, the Reynolds stresses drive a positive flux of angular momentum away from the rotation axis and a negative flux of angular momentum inwards towards the rotation axis. Therefore, in cases with free-slip mechanical boundaries, Reynolds stresses drive two cylindrical zonal flow bands outside the tangent cylinder (Aurnou and Olson, 2001; Christensen, 2001). The outer band along the equator contains a prograde zonal jet. The inner band adjacent to the tangent cylinder contains a retrograde zonal jet. Qualitatively similar flow patterns, with quasicolumnar, prograde equatorial jets, have been found in some of the anelastic hydrodynamic models of solar convection in which $Ra^* \lesssim 0.5$ (e.g., Miesch et al., 2000; Brun and Toomre, 2002).

3.2. The buoyancy-dominated regime

In the $Ra^* \gg 1$ regime, the buoyancy forcing is dominant and the Coriolis force is no longer balanced by induced pressure gradients in the fluid. The Taylor–Proudman constraint is relaxed and vigorous convection can occur via three-dimensional (3D) motions. In our simulations, we find that the convection in this regime occurs predominantly via small-scale, turbulent motions and secondarily via a weaker mean meridional circulation. This is shown schematically in Fig. 3c.

Scorer (1966), Gough and Lynden-Bell (1968) and Bretherton and Turner (1968) first argued that strong mixing will act to homogenize a fluid's angular momentum far from any viscous boundaries. Angular momentum can become well-mixed and homogenized either due to the action of small-scale 3D turbulence or by axisymmetric mean meridional circulations. Flows in which angular momentum becomes homogenized have been simulated in a number of studies of atmospheric and ocean dynamics (Held and Hou, 1980; Allison et al., 1994; Cessi, 1998; Semeniuk and Shepherd, 2001) as well as laboratory experiments (Hopfinger et al., 1982; Zhang et al., 1997). Semeniuk and Shepherd (2001) show that angular momentum homogenization can occur on two time scales. The longer time scale is due to homogenization by large-scale mean meridional circulation, while, in their models, more rapid homogenization occurs due to small-scale inertial adjustment. In the atmospheric dynamics model of Cessi (1998), it is demonstrated that advection effects act to homogenize angular momentum and temperature, while fluid viscosity acts to homogenize zonal velocity and rigid boundaries act to restore the fluid to the planetary rotation rate.

The angular momentum of a parcel of fluid, viewed from an inertial reference frame is called the absolute angular momentum, M, and is defined here as

$$\begin{aligned} M &= M_{\mathrm{ZF}} + M_{\mathrm{PR}} \\ &= \rho u_\phi s + \rho \Omega s^2, \end{aligned} \tag{9}$$

where ϕ denotes azimuth, $s = r\sin\theta$ is cylindrical radius and θ is colatitude. The first term on the right, M_{ZF}, is the angular momentum due to the zonal flow velocity, u_ϕ, of the fluid parcel measured with respect to the rotating reference frame. The second term, M_{PR}, is the angular momentum from rigid body rotation of the parcel due to the planetary rotation. From (9) we deduce that at any location in the fluid shell where $M > M_{\mathrm{PR}}$, the value of M_{ZF} must be positive and, therefore, the zonal flow must be prograde ($u_\phi > 0$). Similarly, locations where $M < M_{\mathrm{PR}}$ must have retrograde zonal flows. In locations where $M = M_{\mathrm{PR}}$, no zonal flows occur.

We nondimensionalize M by the absolute angular momentum of a parcel of fluid moving at the planetary rotation rate (i.e., in rigid body rotation) along the outer boundary equator:

$$\begin{aligned} M^* &= M_{\mathrm{ZF}}/\left(\rho\Omega r_o^2\right) + M_{\mathrm{PR}}/\left(\rho\Omega r_o^2\right) = M^*_{\mathrm{ZF}} + M^*_{\mathrm{PR}} \\ &= Ro\frac{s}{r_o} + \frac{s^2}{r_o^2}. \end{aligned} \tag{10}$$

In the $Ra^* \gg 1$ regime, vigorous mixing homogenizes the fluid layer's (globally-conserved) angular momentum. Because all our calculations start out in rigid body rotation, mixing will tend to produce a spatially-homogeneous M^*-value that equals the volume integral of the initial angular momentum distribution:

$$\begin{aligned} \left\langle M^* \right\rangle_V &= \frac{1}{V}\int_V \left[M^*_{\mathrm{PR}}\right] \mathrm{d}V \\ &= \frac{1}{(4\pi/3)(r_o^3 - r_i^3)} \\ &\quad \times \int_0^{2\pi}\int_0^{\pi}\int_{r_i}^{r_o} \left[\frac{(r\sin\theta)^2}{r_o^2}\right] r^2 \sin\theta \,\mathrm{d}r\,\mathrm{d}\theta\,\mathrm{d}\phi \\ &= \frac{2}{5}\left[\frac{1-\chi^5}{1-\chi^3}\right], \end{aligned} \tag{11}$$

where $\langle \ldots \rangle_V$ indicates averaging over the spherical shell volume, V. For the $\chi = 0.75$ cases investigated in this study, $\langle M^* \rangle_V = 0.528$. Fig. 6 shows the relationship between M^*_{PR} and $\langle M^* \rangle_V$ and the behavior of the zonal flows that develop in a well-mixed $\chi = 0.75$ shell. Close to the rotation axis $\langle M^* \rangle_V$

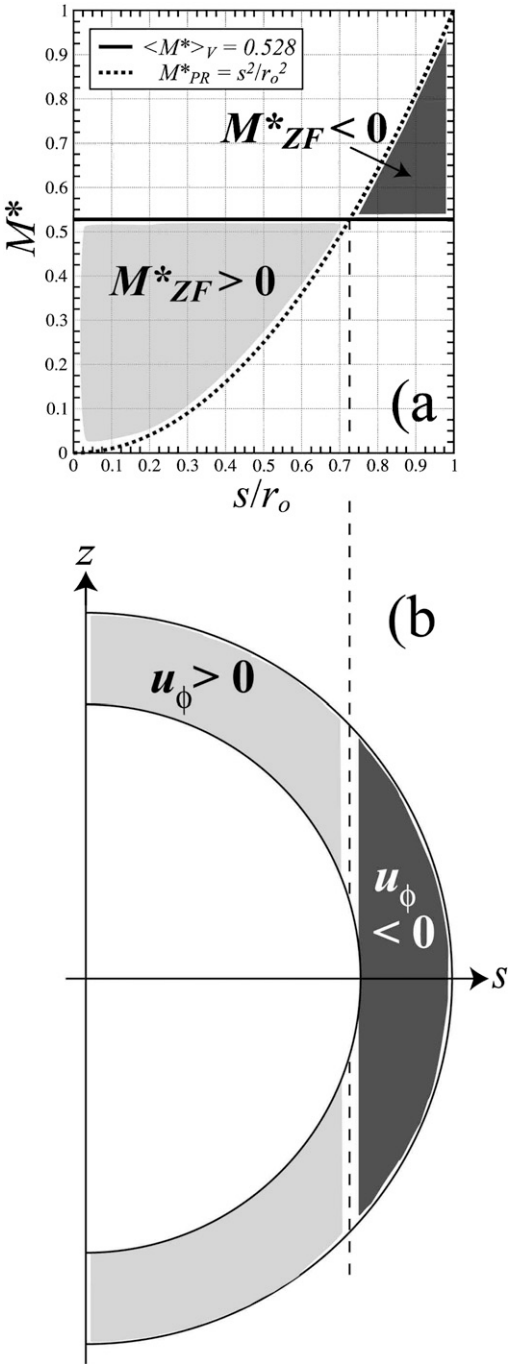

Fig. 6. (a) Profiles of $\langle M^* \rangle_V$ and $M^*_{\rm PR}$ in a homogenized $\chi = 0.75$ spherical shell as a function of cylindrical radius. (b) Schematic showing the corresponding zonal velocities, u_ϕ. Light (dark) gray shading corresponds to prograde (retrograde) zonal velocities.

is greater than $M^*_{\rm PR}$ and $M^*_{\rm ZF} = \langle M^* \rangle_V - M^*_{\rm PR} > 0$. Therefore, the zonal flow is prograde. Beyond the critical cylindrical radius where $\langle M^* \rangle_V = M^*_{\rm PR}$, the value of $M^*_{\rm ZF}$ becomes negative and the zonal flow reverses direction, becoming retrograde.

The zonal velocity field in a convectively-homogenized fluid shell is found from (10) and (11) to vary as

$$Ro = \frac{r_o}{s}\langle M^* \rangle_V - \frac{s}{r_o} = \frac{r_o}{r\sin\theta}\langle M^* \rangle_V - \frac{r\sin\theta}{r_o}. \tag{12}$$

On the outer boundary this becomes

$$Ro(r_o,\theta) = \frac{1}{\sin\theta}\left(\langle M^* \rangle_V - \sin^2\theta\right) = \frac{1}{\sin\theta}\left(\frac{2}{5}\left[\frac{1-\chi^5}{1-\chi^3}\right] - \sin^2\theta\right). \tag{13}$$

Therefore, angular momentum homogenization in a $\chi = 0.75$ shell produces a surface zonal flow profile

$$Ro = \frac{1}{\sin\theta}\left(0.528 - \sin^2\theta\right), \tag{14}$$

similar to Allison et al.'s (1994) Eq. (14). At the equator, the above equation yields $Ro = -0.472$. Further, the zonal velocity will cross through zero at $\pm 43.4°$ latitude, corresponding to $s = 0.727 r_o$.

The solid line in Fig. 7a shows how $\langle M^* \rangle_V$ varies as function of spherical shell radius ratio. Convective mixing extends to greater depths in smaller radius ratio shells, producing lower values of $\langle M^* \rangle_V$. However, the value of $\langle M^* \rangle_V$ remains well below unity even as χ approaches a value of 1 because the high-latitude fluid still contains little angular momentum. This means that angular momentum homogenization in shallow layers is also capable of producing zonal flows similar to those on the ice giants.

Fig. 7b shows the outer boundary zonal velocity, calculated from (13), plotted as a function of latitude for six different values of the radius ratio. Strong retrograde flows occur at low latitudes, while the flow is prograde and becomes infinite at the poles. Polar values of Ro will not actually approach infinity because viscous stresses arise to damp such flows. However, at latitudes away from the polar regions, 3D convective mixing is likely to produce zonal flows that are well-described by (13).

The angular momentum homogenization model provides a number of predictions of zonal flow systematics in Boussinesq fluid layers. The zonal flow Ro values in the $Ra^* \gg 1$ regime should only depend on radius ratio χ and cylindrical radius s. Neither the Ekman number nor the modified Rayleigh number affect the nondimensional zonal velocities in the $Ra^* \gg 1$ regime. Although mixing in deeper layers generates higher amplitude zonal flows, angular momentum mixing is able to generate large amplitude zonal flows irrespective of the depth extent of mixing. The zonal velocity should have the same parabola-like profile in all well-mixed regions and the latitudinal extent of the region of retrograde flow should be proportional to the amplitude of the flow along the equator. Strong polar mixing should lead to strongly prograde high-latitude jets that will be truncated by viscous damping near the poles. Because M varies only as a function of cylindrical radius in Boussinesq fluids, the mean zonal flow will not vary strongly in the axial direction, even though the force balance is far from geostrophic. This also means that the surface zonal flow will be symmetric across the equatorial plane. Such equatorially-symmetric flows differ from the results of some shallow layer models and from the complex banded flows that arise in fully-developed $Ra^* \ll 1$ models.

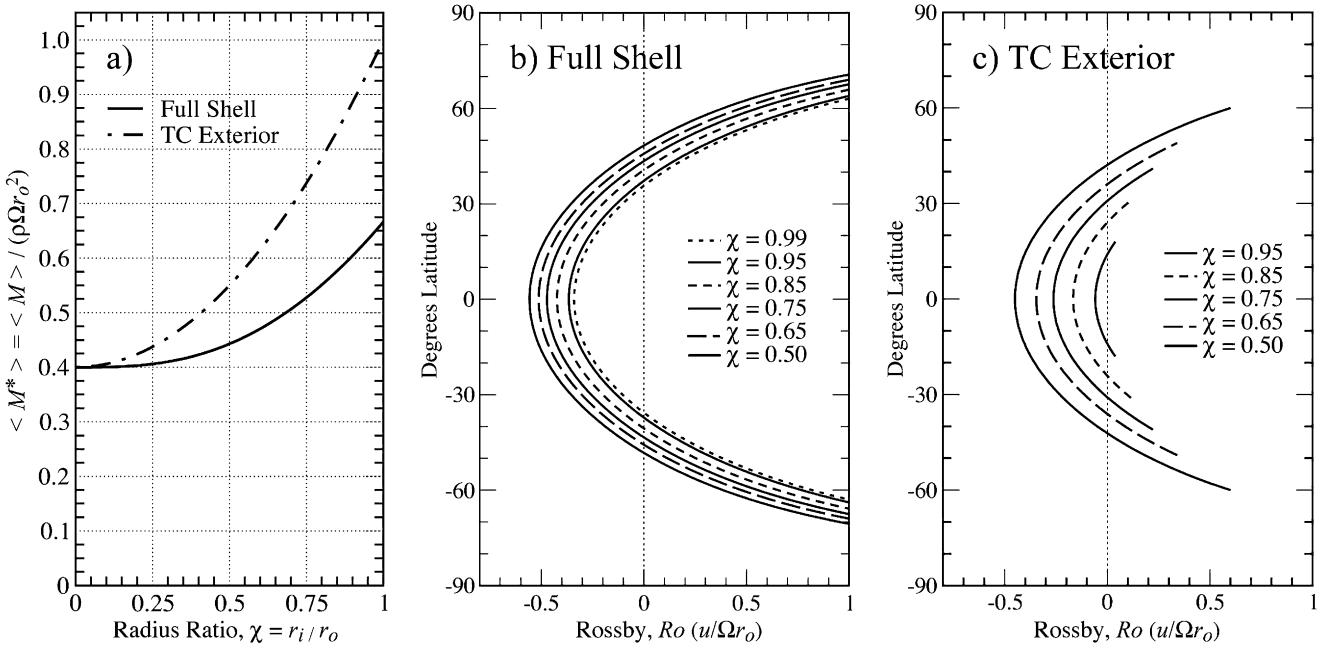

Fig. 7. (a) Homogenized nondimensional absolute angular momentum, $\langle M^* \rangle$, in a Boussinesq fluid layer of spherical shell radius ratio χ. Solid line: Homogenization over the entire spherical shell. Dashed line: Homogenization only over the region exterior to the tangent cylinder. (b) Outer boundary zonal flow $Ro(r_o, \theta)$ for full shell homogenization, plotted as a function of latitude for six different radius ratio values. (c) Outer boundary zonal flow $Ro(r_o, \theta)$ for homogenization only in the region exterior to the tangent cylinder, plotted as a function of latitude for five different radius ratio values.

3.3. The transitional regime

Gilman (1977) and Glatzmaier and Gilman (1982) showed that there is also an intermediate, transitional regime in the vicinity of $Ra^* \simeq 1$. Here, we consider transitional cases to be those in which convective mixing acts to homogenize the fluid's angular momentum in only part of the spherical shell (Fig. 3b). In the $Ra^* \simeq 1$ regime, the strongest convective mixing tends to occur in the equatorial region. In the polar regions, where Coriolis effects are stronger, the $Ra^* \simeq 1$ convection may still be columnar and will be less vigorous. We make the ad hoc assumption that this boundary exists somewhere in the vicinity of the tangent cylinder. Averaging $M^*_{\rm PR}$ over the equatorial region exterior to the tangent cylinder leads to

$$\langle M^* \rangle_{\rm TC} = 1 - \frac{3}{5}\left(1 - \chi^2\right) \tag{15}$$

and surface zonal velocities in the equatorial region of

$$Ro(r_o, \theta) = \frac{1}{\sin\theta}\left(\langle M^* \rangle_{\rm TC} - \sin^2\theta\right). \tag{16}$$

The dashed line in Fig. 7a shows how $\langle M^* \rangle_{\rm TC}$ varies with χ. For $\chi = 0.75$, $\langle M^* \rangle_{\rm TC} = 0.7375$. The $\langle M^* \rangle_{\rm TC}$ values are larger than the corresponding $\langle M^* \rangle_V$ values at the same χ because the transitional regime model does not average over the higher latitude, low M^* fluid near the rotation axis. Therefore, convective mixing of the equatorial fluid alone leads to lower amplitude equatorial flow velocities and narrower equatorial jets than in comparable fully-mixed $Ra^* \gg 1$ cases, as can be seen by comparing the profiles in Figs. 7b and 7c.

4. Results

4.1. Mixed mechanical boundary conditions

The results of our numerical simulations demonstrate that convection in a spherical shell can occur in the three zonal flow regimes discussed above. In the $Ra^* \ll 1$ regime, cylindrical, quasigeostrophic flow produces strong prograde equatorial jets, similar to those observed on Jupiter and Saturn. In the transitional $Ra^* \sim 1$ regime and the $Ra^* \gg 1$ regime, the equatorial zonal flow is retrograde and better simulates the observed winds on Uranus and Neptune.

Three mixed mechanical boundary condition cases are carried out to illustrate the different regimes of deep convection driven zonal flow. Using a fixed standard Rayleigh number of $Ra = 10^7$ and varying Ekman numbers of $E = 10^{-4}$, 3×10^{-4} and 10^{-3}, these cases correspond to modified Rayleigh numbers of $Ra^* = 0.1$, 0.9 and 10, respectively. Fig. 8 shows instantaneous patterns of velocity and temperature from these cases. The panels in the left-hand column show meridional slices of the azimuthally-averaged velocities. The left half of the panel shows the poloidal flow with blue (yellow) contours representing counterclockwise (clockwise) meridional circulation. The panel's right half shows azimuthal velocity with red (blue) representing prograde (retrograde) flow. The panels in the central column display temperature contours in the equatorial plane, viewed from above. Red (blue) contours represents hot (cold) fluid. The panels in the right-hand column show the azimuthal velocity on the outer boundary, r_o. The azimuthal velocities in the corresponding left-hand and right-hand panels have identical color scales.

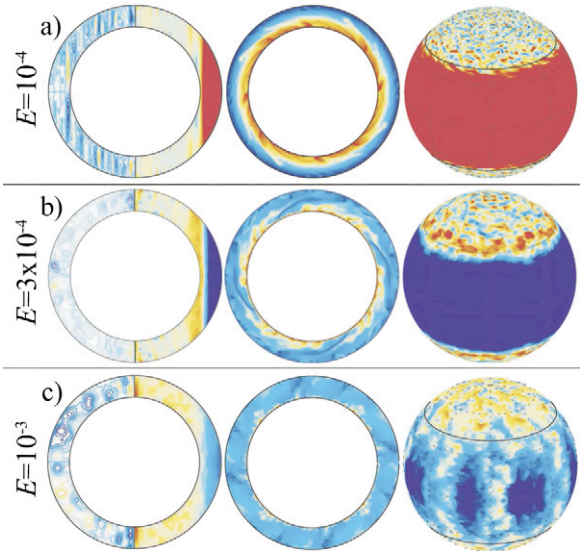

Fig. 8. Instantaneous flow and temperature fields for mixed mechanical boundary condition cases with $Ra = 10^7$, $Pr = 1$, $\chi = 0.75$ and varying Ekman number values. Row (a) $E = 10^{-4}$ ($Ra^* = 0.1$); row (b) $E = 3 \times 10^{-4}$ ($Ra^* = 0.9$); and row (c) $E = 10^{-3}$ ($Ra^* = 10.0$). The panels in the left-hand column show meridional slices of the azimuthally-averaged flow field with poloidal velocity shown on the left and azimuthal velocity shown on the right. Blue (yellow) contour lines denote counterclockwise (clockwise) flow. Red (blue) azimuthal flow is prograde (retrograde). The panels in the middle column show temperature contours in the equatorial plane viewed from above. Reds (blues) show hot (cold) fluid. The right-hand column of panels shows the azimuthal velocity on the outer boundary. Contour intervals are determined individually for each case.

Fig. 8a shows the results from the $Ra^* = 0.1$ case. The quasigeostrophic convection generates quasi-2D motions that are closely aligned with the rotation axis. The strong prograde tilt of the convection columns, shown in the equatorial temperature contours, generates the Reynolds stresses that drive the prograde flow in the equatorial region. At higher latitudes inside the tangent cylinder, small-scale convective structures generate weak, time-variable zonal flows.

Results from the $Ra^* = 0.9$ case are shown in Fig. 8b. The zonal flow has reversed and is retrograde throughout much of the equatorial region. The meridional flow retains little of the columnar structure visible in the $Ra^* = 0.1$ case. Instead, small-scale meridional cells exist throughout the shell. However, the temperature isotherms show that plumes leaving the inner boundary remain nearly intact upon traversing the shell. Because the flow is not geostrophic, the plume is deflected in the retrograde direction by the Coriolis force. There also appears to be a well-defined tangent cylinder separating the low-latitude from the high-latitude flow fields. This tangent cylinder structure is most likely due to the excessive damping of the high-latitude zonal flows in mixed cases.

Fig. 8c shows the results of the $Ra^* = 10$ case. The zonal flow still varies primarily as a function of cylindrical radius in this case. However, there is no signature of a well-defined tangent cylinder. The turbulent, 3D convection that develops in this case produces thin thermal boundary layers. Thermal plumes are unable to traverse the fluid layer intact.

Latitudinal profiles of the azimuthally-averaged zonal flow on the outer boundary are plotted in Fig. 9a for the $Ra = 10^7$ cases. The solid line denotes the $E = 10^{-4}$ ($Ra^* = 0.1$) case; the long-dashed line denotes the $E = 3 \times 10^{-4}$ ($Ra^* = 0.9$) case; the short-dashed line denotes the $E = 10^{-3}$ ($Ra^* = 10$) case. In the $E = 10^{-4}$ case, a well-developed prograde equatorial jet forms in the equatorial region. The two higher E cases develop retrograde equatorial jets that are similar in amplitude and spatial structure. The $E = 3 \times 10^{-4}$ and the $E = 10^{-3}$ cases have equatorial Ro-values of approximately -0.3 and -0.34, respectively. These are both larger than the idealized tangent cylinder mixing model value of $Ro = -0.26$ from (16), which one might expect to apply in cases with mixed mechanical boundary conditions. These two cases also develop complex zonal flow structures inside the tangent cylinder. In the $E = 3 \times 10^{-4}$ case, these structures are time-dependent, vacillating features of the flow, whose steady component contains little energy. In the $E = 10^{-3}$ case, the prograde jets are nonzero after time-averaging and likely result from the interplay of M^*-homogenization effects and high-latitude viscous stresses.

Fig. 9b shows equatorial plane temperature profiles for the three $Ra = 10^7$ cases. The $E = 10^{-4}$ case has a quasilinear conductive temperature profile, except near r_i where a thermal

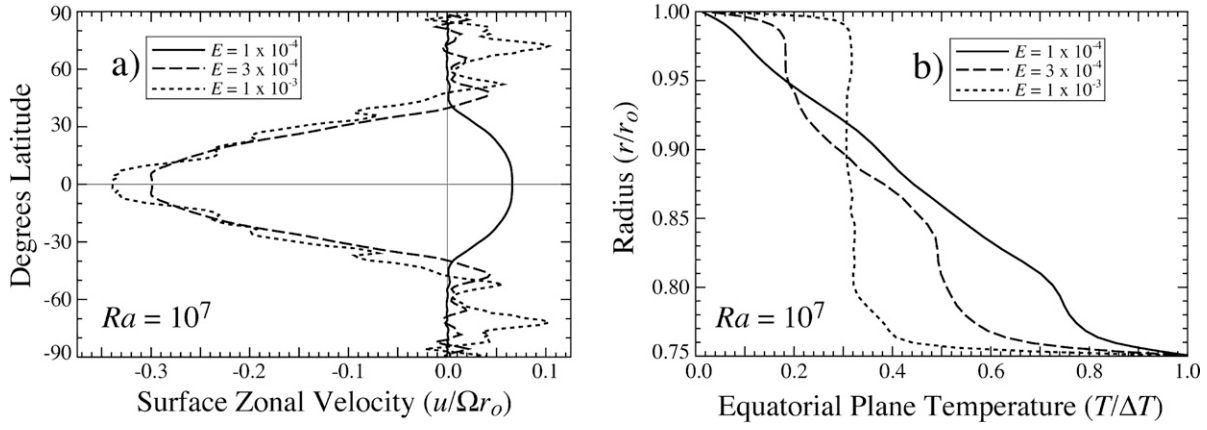

Fig. 9. Cases with $Ra = 10^7$, $Pr = 1$, mixed mechanical boundary conditions and $E = 10^{-4}$, 3×10^{-4} and 10^{-3}. These E values correspond, respectively, to $Ra^* = 0.1$, 0.9 and 10. (a) Latitudinal profiles of zonal wind velocity given in Ro units. (b) Equatorial temperature profiles.

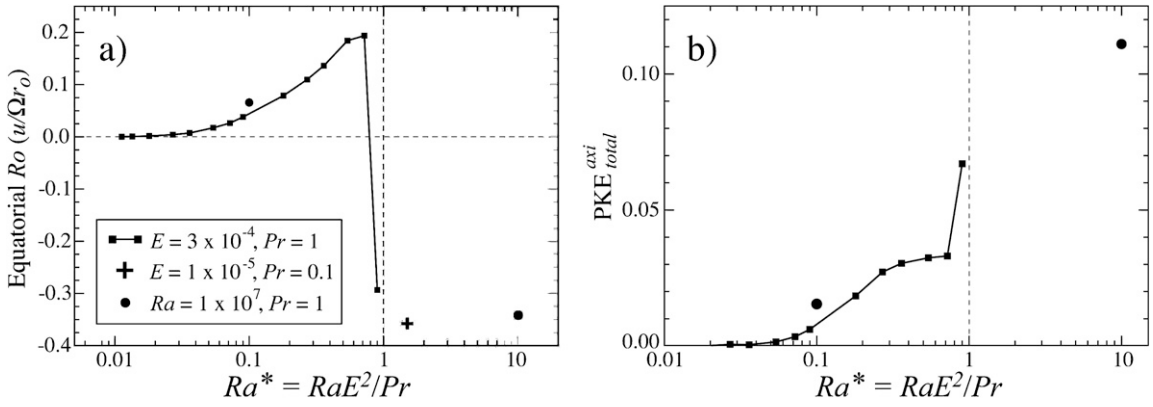

Fig. 10. (a) Maximum equatorial jet zonal wind velocity (in *Ro* units) plotted versus modified Rayleigh number, Ra^*. As Ra^* approaches unity, the jet direction reverses. (b) The ratio of the axisymmetric and the total poloidal kinetic energies, $\mathrm{PKE}^{\mathrm{axi}}_{\mathrm{total}}$, plotted as a function of modified Rayleigh number, Ra^*.

boundary layer has developed. The temperature profile for the $E = 3 \times 10^{-4}$ case has a well-developed boundary layer near r_i and a weak thermal boundary layer by r_o. In the $E = 10^{-3}$ case, the convection is fully-developed throughout the shell. Sharp thermal boundary layers exist at r_i and r_o and the fluid interior is isothermalized by the strong convective mixing.

In order to determine in greater detail how deep convective zonal flows change with Ra^*, we have carried out a suite of mixed calculations at $E = 3 \times 10^{-4}$. Fig. 10a shows the equatorial Rossby number plotted as a function of modified Rayleigh number, Ra^*, for all our calculations. The calculations with $E = 3 \times 10^{-4}$ are plotted as square symbols. The two solid circles correspond to the two cases with $Ra = 10^7$ and $E = 10^{-3}$ and 10^{-4}. The plus symbol corresponds to the free-slip boundaries case described in Section 4.2. In cases with $0.01 \leqslant Ra^* \leqslant 0.8$, the equatorial jet Rossby number is positive and increases in value with Ra^*, corresponding to a prograde equatorial jet. The direction of the equatorial jet reverses at $Ra^* = 0.9$, producing a retrograde flow with equatorial $Ro \sim -0.3$. For the three cases shown with $Ra^* > 1$, the equatorial flow is retrograde with $Ro \sim -0.3$ to -0.36. The sharpness of the change from prograde to retrograde equatorial flow suggests that this is transition may occur by way of a transcritical bifurcation. A sharp transition between nonrotating and rotation dominated flow has also been observed in the grid turbulence experiments of Hopfinger et al. (1982).

Fig. 10b plots the ratio of the azimuthally-averaged poloidal kinetic energy and the total poloidal kinetic energy, $\mathrm{PKE}^{\mathrm{axi}}_{\mathrm{total}}$, as a function of Ra^*. This ratio corresponds to the strength of the mean meridional circulation with respect to the total poloidal energy in the flow. For $Ra^* < 0.8$, this ratio grows smoothly with Ra^*. It then jumps in value from roughly 3.5 to 6% at $Ra^* = 0.9$, where the equatorial flow reverses direction. At $Ra^* = 10$, the ratio increases to a value of roughly 11%. These relatively low values indicate that the energy in the mean meridional circulation remains weak even for large Ra^*-values.

4.2. Free-slip mechanical boundaries

The high Ra^* mixed cases presented in the previous section generate strong retrograde equatorial flows, but do not reproduce strong prograde high-latitude jets similar to those observed on Uranus and Neptune. However, Fig. 4 shows that a free-slip inner boundary allows stronger, larger-scale high-latitude zonal flows to develop. Therefore, we have carried out a $Ra^* = 1.5$ calculation using free-slip conditions on both boundaries to generate a surface zonal flow profile that better approximates those observed on the ice giants.

Fig. 11 shows time series of the (dimensionless) kinetic energies from the free-slip calculation. In order to keep this run numerically stable, we raised the Rayleigh number in discrete steps up to its final value of $Ra = 1.5 \times 10^9$. Fig. 11 starts at the time of this final step increase at $t = 0.16194$ viscous time scales. There is a transient after the Ra increase that lasts for roughly 0.1 viscous time scales (i.e., ~1600 rotations at $E = 10^{-5}$). By $t \simeq 0.18$ time scales, the poloidal energy is quasi-steady, whereas the toroidal energy is still increasing (Figs. 11a and 11b). However, the system appears to have reached a dynamically quasisteady state since the ratio of axisymmetric to total poloidal energy, $\mathrm{PKE}^{\mathrm{axi}}_{\mathrm{total}}$, and the ratio of axisymmetric to total toroidal energy, $\mathrm{TKE}^{\mathrm{axi}}_{\mathrm{total}}$, are both stationary at the end of the integration (Fig. 11c).

Output parameters for the free-slip case are given in Table 3. The values of total kinetic energy density KE, the poloidal-toroidal energy ratio KE^P_T, and the minimum and maximum surface Rossby numbers are given at the end of the integration at $t = 0.21448$ viscous diffusion time scales. The axisymmetric poloidal and toroidal energy fractions, $\mathrm{PKE}^{\mathrm{axi}}_{\mathrm{total}}$ and $\mathrm{TKE}^{\mathrm{axi}}_{\mathrm{total}}$, are averaged from $t = 0.18$–0.21 diffusion times. Note that over 99% of the total kinetic energy is contained within the toroidal flow field. Furthermore, the axisymmetric part of the toroidal flow contains over 99% of the total toroidal energy. In contrast, the axisymmetric component of the poloidal energy contains around 32% of the total poloidal energy. The non-zonal, turbulent convective motions contain roughly twice as much energy as the mean meridional circulation and have an typical Reynolds number of about 8×10^4, based on the shell depth and the rms nonzonal, poloidal flow velocity. The turbulent convection also effectively transfers heat across the fluid layer. The Nusselt number, which is the ratio of total heat transfer to conductive heat transfer, is $Nu = 29.5 \pm 0.5$ averaged over $t = 0.18$–0.21.

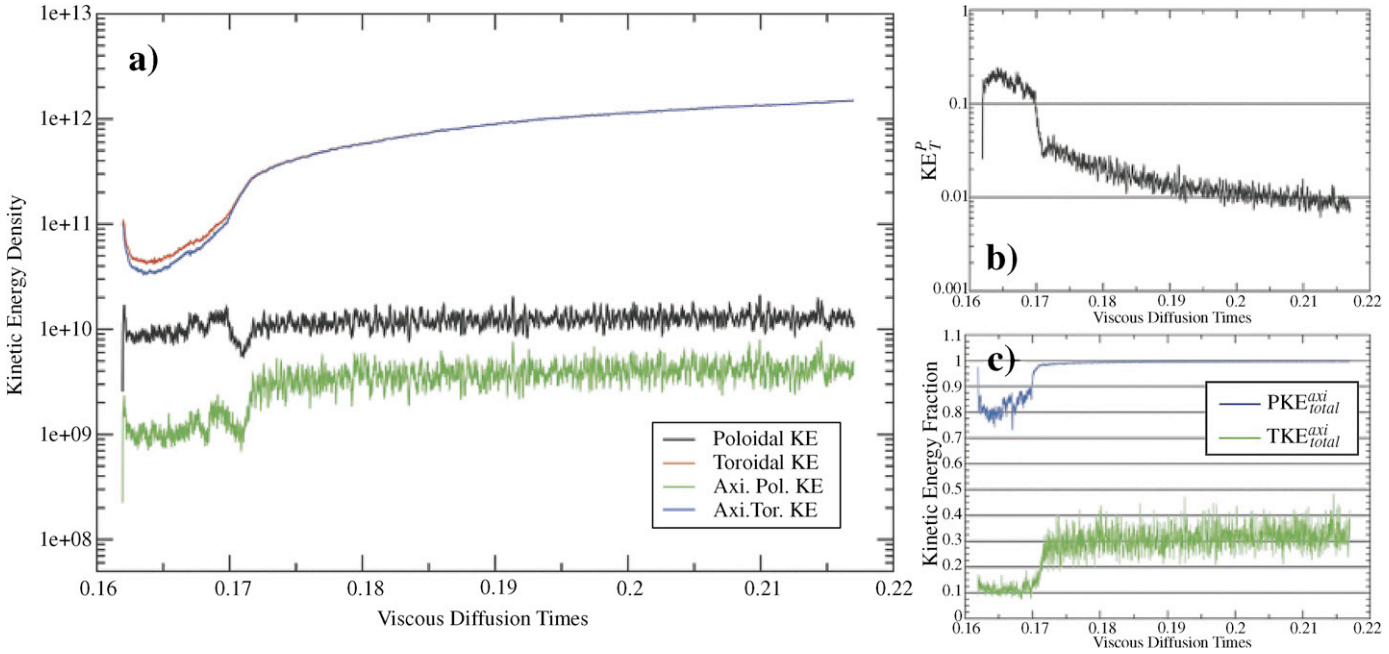

Fig. 11. (a) Time series of nondimensional kinetic energy components for the free-slip mechanical boundaries case. The free-slip case was re-started at a number of *Ra*-values until the final value of 1.5×10^9 was reached at $t = 0.16194$ viscous diffusion times. (a) Time series of the $Ra = 1.5 \times 10^9$ kinetic energy densities for the different components of the flow field. (b) Time series of the poloidal–toriodal kinetic energy ratio. (c) Time series of the axisymmetric-total kinetic energy ratios for the poloidal flow fields (green) and the toroidal flow fields (blue). Note that the toroidal energy component has not yet equilibrated at the end of the calculation at $t = 0.21448$. Although the toroidal energy is still slowly increasing at $t = 0.21448$, the energy ratios have reached quasisteady values.

Table 3
Nondimensional outputs parameters from the free-slip boundaries case

KE	KE_T^P	TKE_{total}^{axi}	PKE_{total}^{axi}	Max[$Ro(r_o)$]	Min[$Ro(r_o)$]	*Nu*
1.51×10^{12}	0.009	0.9974 ± 0.0004	0.32 ± 0.04	+0.85	−0.38	29.5 ± 0.5

KE is the volume averaged kinetic energy density. KE_T^P is the ratio of poloidal and toroidal energies. TKE_{total}^{axi} is the ratio of axisymmetric and total toroidal energies. PKE_{total}^{axi} is the ratio of axisymmetric and total poloidal energies. The fifth and sixth columns give the maximum and minimum values of the Rossby number on the outer boundary. The last column gives the Nusselt number, *Nu*, which is the nondimensional heat transfer across the shell. Variances are given when values have been averaged from $t = 0.18$ to the end of the integration at $t = 0.21448$ viscous diffusion times. Values without associated variances correspond to $t = 0.21448$.

Fig. 12 displays velocity profiles and meridional snapshots from the free-slip case. Fig. 12a shows azimuthally-averaged zonal velocity profiles on the outer boundary at three different times during the calculation. The velocities are similar in structure to those observed on Uranus and Neptune, although the *Ro* values are larger than the observed values. The strong retrograde jet in the equatorial region is relatively steady in time, smooth in spatial structure and symmetric across the equatorial plane. The equatorial velocity is $Ro \simeq -0.36$. In contrast, the prograde high-latitude jets increase in strength and have a good deal of small-scale structure. The meridional slice shown in Fig. 12b shows color contours of the azimuthally-averaged zonal velocity and streamlines of the azimuthally-averaged poloidal flow at $t = 0.21448$. The structure of the azimuthal velocity varies primarily as a function of cylindrical radius. At high-latitudes, the flow becomes well organized by Coriolis forces; the thermal structures above ∼70° latitude show strong axial alignment in Fig. 12c. The averaged axial vorticity contours, displayed in Fig. 12d, show that turbulent angular momentum mixing produces spatially-variable, weakly negative axial vorticity at low latitudes. At latitudes poleward of ±80°, rotationally-organized flow produces strong, positive vortices. Therefore, this $Ra^* = 1.5$ free-slip case is in the transitional regime: buoyancy driven flow occurs at lower latitudes and Coriolis dominated flows develop near the poles.

4.3. Analysis of high Ra cases*

The theoretical models in Sections 3.2 and 3.3 describe $Ra^* \gtrsim 1$ zonal flows in terms of angular momentum homogenization processes. In Fig. 13 we test these models using the results of the free-slip case, in which angular momentum is globally conserved. (In contrast, rigid mechanical boundaries can act as a source or sink of angular momentum.) Fig. 13a shows latitudinal profiles of azimuthally-averaged zonal velocity on r_o and r_i at $t = 0.17706$ and $t = 0.21448$ viscous diffusion times. The equatorial flows are nearly identical at $t = 0.17706$ and $t = 0.21448$. The high-latitude jets, driven by relatively weak high-latitude quasigeostrophic Reynolds stresses, increase in strength by ∼85% over this time interval. Quasigeostrophic Reynolds stress driven flows are balanced by large-scale viscous stresses and tend to equilibrate on the viscous diffusion

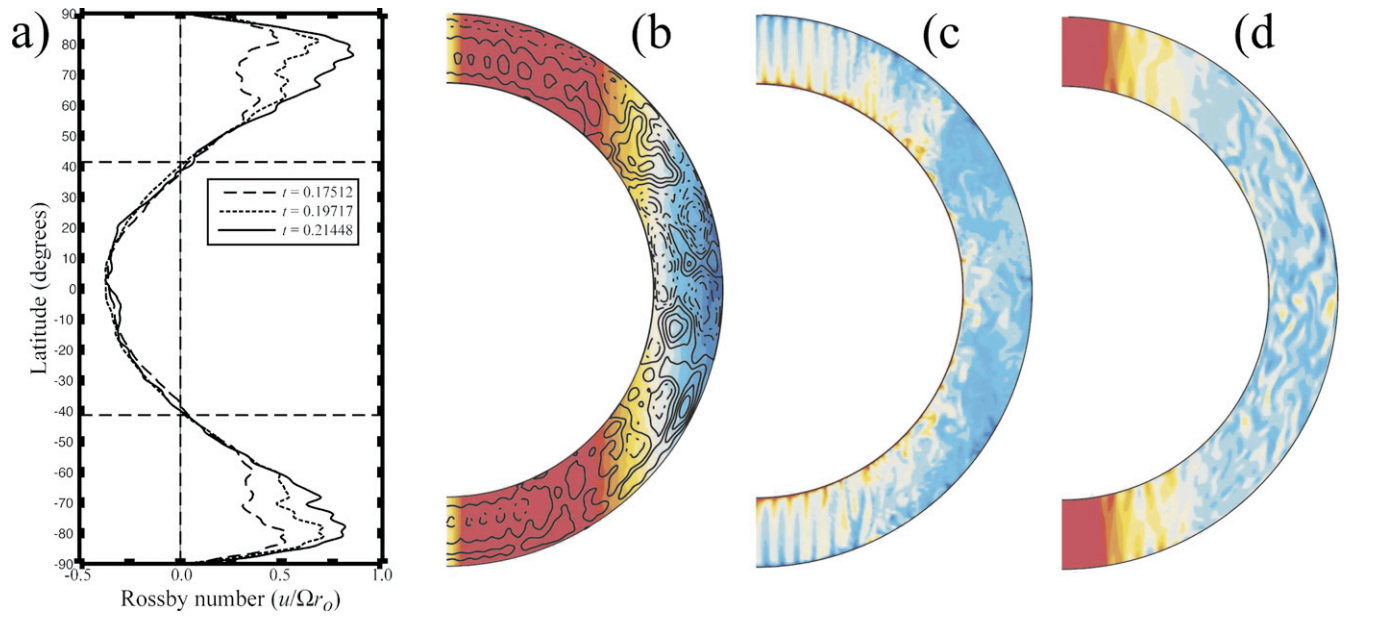

Fig. 12. Snapshots from free-slip boundaries case. (a) Outer boundary average zonal wind profiles at $t = 0.17512$, 0.19717 and 0.21448 viscous diffusion times. (b) Meridional slice showing contours of azimuthally-averaged azimuthal velocity and streamlines of poloidal flow. (c) Meridional slice of azimuthally-averaged temperature. The contouring scheme is the same as in earlier figures. (d) Meridional slice of azimuthally-averaged axial vorticity. Red (blue) contours denote positive (negative) contours of axial vorticity.

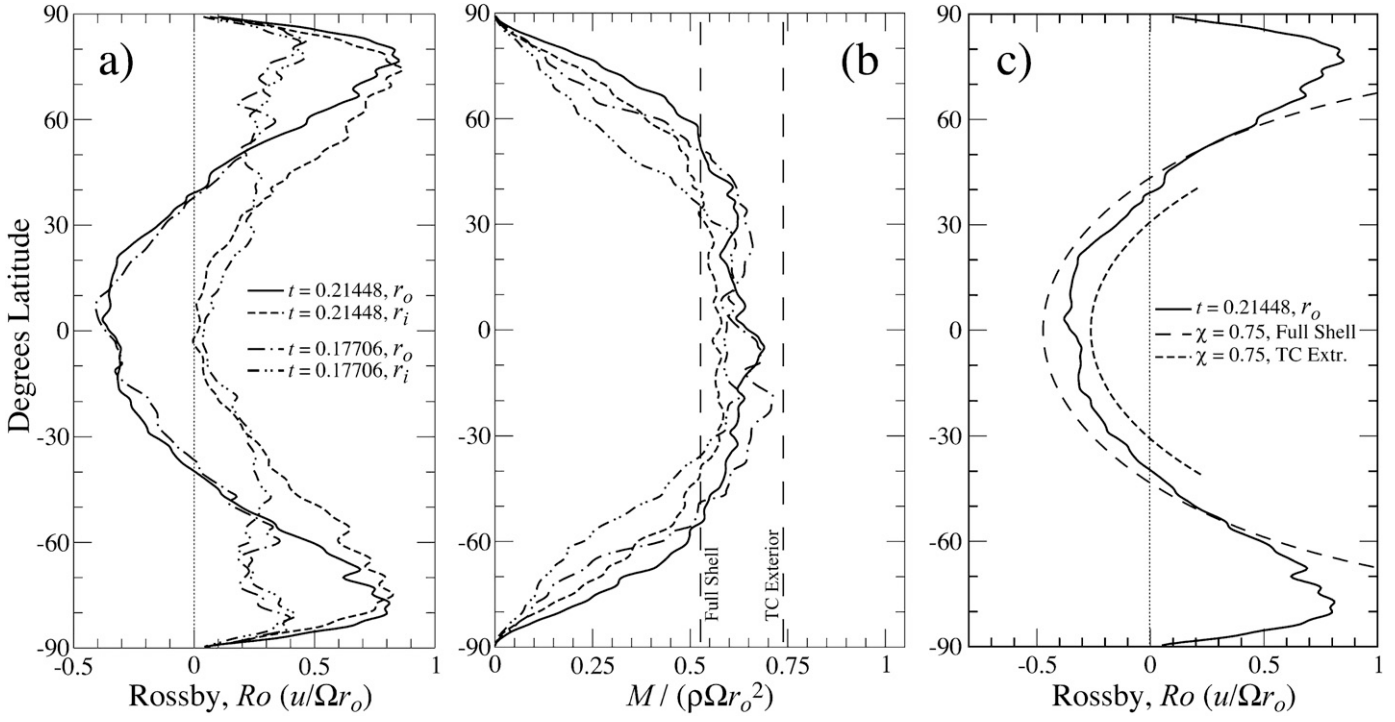

Fig. 13. (a) Azimuthally-averaged zonal velocity profiles from the free-slip case plotted as a function of latitude on the outer boundary (solid and dot-dashed lines) and on the inner boundary (dashed and double dot-dashed lines). The profiles are from the solutions at $t = 0.21448$ and $t = 0.17706$ viscous diffusion times. (b) The same velocity data as in panel a, but plotted in terms of nondimensional absolute angular momentum, $M^* = M^*_{\rm ZF} + M^*_{\rm PR}$. For comparison, the long-dashed vertical lines denote the fully-homogenized $\langle M^* \rangle_V = 0.528$ case and the transitional $\langle M^* \rangle_{\rm TC} = 0.7375$ case. (c) Outer boundary averaged zonal velocity at $t = 0.21448$ plotted versus the theoretical outer boundary zonal flow profile for angular momentum homogenization of the full shell volume (long-dashed line) and for angular momentum homogenization of the region exterior to the tangent cylinder (short-dashed line).

time scale (Christensen, 2002). In contrast, zonal flows controlled by M^*-homogenization equilibrate on the much shorter advective time scale. The increasing velocities of the high-latitude jets minimally affect the equatorial zonal flows because little angular momentum is carried by fluid near the rotation axis.

Fig. 13b shows the zonal velocities from Fig. 13a recast in terms of M^*. The M^* profiles are all roughly constant from $\pm 50°$ latitude, providing support for the angular momentum homogenization concept. Averaged over $\pm\theta_{TC}$, the value of M^* is 0.60 ± 0.05. This value lies between the theoretical values of $\langle M^* \rangle_V = 0.528$ for complete M^*-homogenization in the shell and $\langle M^* \rangle_{TC} = 0.7375$ for mixing only in the equatorial region. These two values, which are demarcated in the figure by the vertical, long-dashed black lines, bracket the M^* profiles in the convectively well-mixed lower latitudes. The profiles in Figs. 13a and 13b agree well with the strongly homogenized, weak boundary drag case of Cessi (1998).

Fig. 13c provides a direct comparison of the free-slip case's outer boundary zonal velocity profile and the theoretical angular momentum homogenization models. The free-slip case is the solid line. The long-dashed line is the profile for full-shell angular momentum homogenization, whereas the short-dashed line denotes the case of mixing only exterior to the tangent cylinder. The free-slip profile lies roughly midway between the two theoretical profiles in the equatorial region, demonstrating that the zonal flow results from angular momentum homogenization in the turbulent region of the shell.

A comparison of the $Ra^* = 0.9$ mixed boundaries case and the $Ra^* = 1.5$ free-slip case shows that their flow fields are qualitatively different, although, based on Ra^* alone, one might expect them to both lie in the transitional regime. No rotationally-organized flow structures exist in the $Ra^* = 0.9$ case, whereas they dominate the polar flow in the $Ra^* = 1.5$ case. In addition, the amplitude of the equatorial jet in the free-slip case is ~25% stronger than in the $Ra^* = 0.9$ mixed case. These differences are due to the stronger viscous effects that arise in the mixed boundary condition case. The effects of the rigid lower boundary and an Ekman number 30 times higher than in the free-slip case both act to release the Taylor–Proudman constraint. This explains the lack of axial polar flow structures in the $Ra^* = 0.9$ mixed case. In addition, the increased viscous effects act to lessen the zonal flow amplitudes in the mixed case.

5. Discussion

5.1. Comparison of models and zonal flow observations

Comparison of Figs. 1, 2, 12a and 14 shows that our free-slip model generates an equatorial zonal flow pattern similar to shallow layer models and the ice giant observations. The agreement between our convection models and shallow layer models in the equatorial region may be due to angular momentum homogenization in the shallow layer models in the vicinity of the equator, where the Coriolis force goes to zero. At higher latitudes, the zonal flow in our free-slip model qualitatively differs from the Rhines scale structures that develop in the shallow layer models. Unfortunately, the high-latitude zonal flows on the ice giants are effectively unconstrained by observations. When such observations become available, it should be possible to discriminate which model better fits the high-latitude zonal flows.

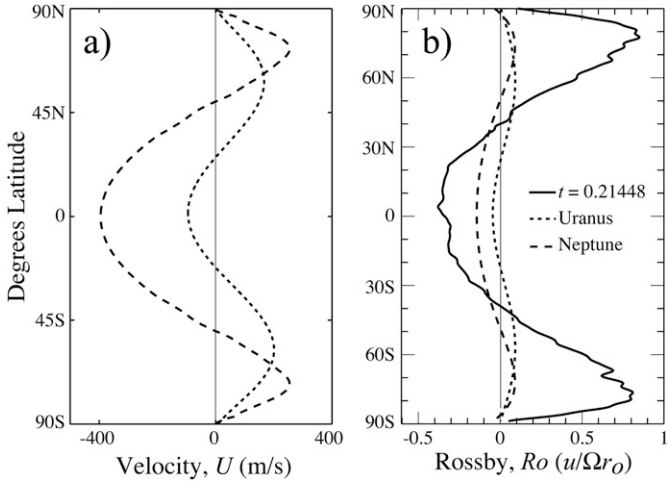

Fig. 14. Surface zonal velocity profiles plotted in (a) m/s and (b) Rossby number units, *Ro*. Solid line: free-slip case at $t = 0.21448$. Short-dashed line: Uranus observation-based model of Hammel et al. (2001). Long-dashed line: Neptune observation-based model of Sromovsky et al. (1993).

The Rossby number amplitudes in our deep convection models are almost an order of magnitude greater than the observational values for the ice giants, as shown in Fig. 14b. The differences in *Ro* amplitude occur for two reasons. First, our $\chi = 0.75$ models likely overestimate the depth of convection on the ice giants. Suomi et al. (1991) argue that deep convection on Neptune occurs down to depths no greater than 2000–3000 km. This depth range corresponds to radius ratio values between 0.88 and 0.92, which differ substantially from the $\chi = 0.75$ radius ratio used in this study. Figs. 7a and 7b show that the amplitudes of the surface zonal flow *Ro* increases with the depth of convective mixing. Thus, our smaller radius ratio models (i.e., deeper convection zones) will tend to produce overly large surface *Ro* amplitudes. Second, the following arguments suggest that compressible models would generate smaller amplitude *Ro* values. In Boussinesq fluids, the ambient fluid density is constant so the angular momentum increases as a function of cylindrical radius alone, $M^*_{PR} = s^2/r_o^2$. In a planetary atmosphere, the fluid density decreases in the radial direction approximately as $\rho(r) = \rho_o \exp[(r_o - r)/H_\rho]$, such that $M^*_{PR} = [\rho(r)/\rho_o](s/r_o)^2$, where H_ρ is the density scale height. This density gradient causes the rigid body angular momentum to increase inward with depth, while the $(s/r_o)^2$ term causes it to increase outward with cylindrical radius. Thus, the $\rho(r)$ and s^2 gradients oppose one another, leading to smaller spatial variations in M^*_{PR} in compressible models. Homogenization in compressible models will then produce $\langle M^* \rangle$ values that differ less from M^*_{PR} than comparable Boussinesq models and are likely to produce smaller amplitude zonal flows.

The angular momentum homogenization model makes numerous predictions concerning the behavior of zonal flows. If we directly apply this model to the ice giants, then it is possible to make predictions concerning mixing processes on these planets based on the surface zonal wind observations. On Uranus, the speed and latitudinal extent of the retrograde equatorial jet are less than on Neptune (Fig. 1). This suggests that mixing

occurs in a deeper layer on Neptune than on Uranus, in agreement with the analysis of Suomi et al. (1991). Note in Fig. 1b that Uranus and Neptune have comparable parabolic equatorial zonal flow profiles, but with stronger retrograde equatorial flow on Neptune. This is also consistent with the angular momentum homogenization framework, assuming deeper mixing occurs on Neptune.

5.2. Comparison of model and planetary heat fluxes

A check on our Boussinesq deep convection model can be made by comparing the measured thermal emissions from the ice giants and the outer boundary heat flux from our $E = 10^{-5}$, free-slip case. From Voyager 2 measurements, the average internal heat flux from Neptune has been inferred to be 433 ± 46 mW/m^2 and for Uranus it is inferred to be 42 ± 47 mW/m^2 (Hubbard et al., 1995; Guillot, 2005). [However, Marley and McKay (1999) have argued that Uranus' internal heat flux must exceed 60 mW/m^2 to explain tropospheric temperature measurements.] Approximate estimates of the adiabatic heat flux give ~10 mW/m^2 for the ice giants. Since the internal heat fluxes for both planets exceed the adiabatic heat flux, deep convection is likely to occur on both Uranus and Neptune. However, it is not clear whether or not this convection occurs in the $Ra^* \gtrsim 1$ regime. In order to compare the observed heat flux values with our $Ra^* \sim 1$ models, we will scale the free-slip case's convective heat flux using neptunian parameter value estimates and available scaling laws for turbulent rotating convective heat transfer taken from the study of Liu and Ecke (1997).

The total heat flux in our Boussinesq model approximates the superadiabatic heat flux carried by convection in the deep atmospheres of the ice giants. By assuming $Ra^* \sim 1$ on Neptune, Eq. (5) yields

$$\Delta T = \left(\frac{\Omega^2 D}{\alpha g_o}\right) Ra^* \sim 2 \text{ K}, \tag{17}$$

where we take the mid-layer thermal expansion coefficient to be $\alpha \sim 10^{-3}$ K^{-1}, $g_o = 11.2$ m/s^2, $\Omega = 2\pi/16.11$ h $= 1.08 \times 10^{-4}$ s^{-1} and a fluid layer thickness of $D = 0.1 r_o = (1 - \chi) r_o = 2500$ km based on the $\chi = 0.90$ estimate of Suomi et al. (1991). Note that this ΔT represents the superadiabatic temperature difference across the entire deep convection fluid layer, including the thermal boundary layers. It is not representative of typical temperature perturbations in the fluid interior, which are small outside the boundary layers (similar to the $E = 10^{-3}$ case in Fig. 9b). Estimating the mean density to be $\rho = 10^2$ kg/m^3, specific heat capacity $C_p = 10^4$ J/(kg K) and thermal diffusivity $\kappa = 10^{-5}$ m^2/s gives a thermal conductivity estimate of $k = \rho C_p \kappa \simeq 10$ W/(m K). These values give a superadiabatic *conductive* heat flux of $Q_{\text{cond}} = k \Delta T / D \sim 10^{-6}$ W/m^2.

In order to estimate our model's superadiabatic *convective* heat flux at planetary parameter values, we use the heat transfer scaling law of Liu and Ecke (1997). They find in experiments using water that for $E \gtrsim 10^{-5}$ and $0.1 \leqslant Ra^* \leqslant 1.5$ that

$$Nu \sim Ra^{2/7} \tag{18}$$

for fixed Ra^* values. For fixed $Ra^* \sim 1$ and $Pr \sim 0.1$, we can rewrite the above scaling as

$$Nu \sim \left(\frac{Ra^* Pr}{E^2}\right)^{2/7} \sim E^{-4/7}. \tag{19}$$

Since the Nusselt number is approximately 30 in the free-slip case, Eq. (19) leads to an estimate for the planetary Nu value of

$$Nu_{\text{planet}} \sim Nu_{\text{model}} \left(\frac{E_{\text{model}}}{E_{\text{planet}}}\right)^{4/7} \sim 30 \left(\frac{10^{-5}}{10^{-15}}\right)^{4/7} \sim 10^7. \tag{20}$$

Thus, the extrapolation of the free-slip case gives an estimated superadiabatic heat flux of $Q_{\text{conv}} \sim 10^7 Q_{\text{cond}} \sim 10$ W/m^2. Since this Q_{conv} estimate greatly exceeds estimates of heat flow along the adiabat, our free slip model predicts that the total internal heat flux necessary to drive $Ra^* \gtrsim 1$ deep convection on the ice giants is of order 10 W/m^2. This estimate is roughly 20 times and 200 times the internal heat fluxes inferred for Neptune and Uranus, respectively.

There are a number of uncertainties that underly the above heat flux estimate. These include uncertainties in interior models of the ice giants, material properties estimates, scaling laws for rotating convective heat transfer and applying Boussinesq models to compressible atmospheres. Taking all these uncertainties into account, it seems plausible that the observed heat fluxes on the ice giants can drive deep atmospheric convection in the $Ra^* \sim 1$ regime.

Despite the uncertainties noted above it is clear that our model results in a rather high estimate of the heat flow. Since the convective heat flux is inversely proportional to the Ekman number $E = \nu/\Omega D^2$, an effective way to obtain a lower heat flow estimate is to invoke smaller layer thickness D. Nevertheless, we argue here that while turbulent angular momentum mixing is likely to be applicable to the ice giants, it is unlikely that zonal flow occurs only in a thin layer because it is difficult to truncate a strong, turbulent zonal flow at shallow to moderate depths. In order to slow down the zonal flow an opposing torque must overcome vertical shear in the turbulent zonal flow. A known mechanism for such a braking torque does not exist in the molecular envelopes of the ice giants. At greater depth, within the ionic liquid layer, the Lorentz force could slow the flow via electromagnetic braking. However, since these regions are predicted to have relatively low electrical conductivities, they may also prove ineffective at truncating strongly turbulent mixing processes. Thus, it seems likely that strong zonal flows occur in, and may even extend below, the full depth of the deep molecular atmospheres of Uranus and Neptune.

It should also be noted that any source of turbulent mixing that homogenizes the fluid's angular momentum can produce zonal flows similar to those generated by our $Ra^* \sim 1$ thermal convection models. Additional mixing mechanisms, including tropospheric turbulence (Showman et al., 2006), compositionally-driven convection (Smith and Gierasch, 1995), and turbulence due to inertial waves, tidal resonances and elliptical instabilities (Kerswell, 2002), may also be worth consideration.

Future simulations should be carried out to determine how heat transfer in Boussinesq convection models varies in cases using more extreme, planetary-like parameter values. These results should be compared to 3D compressible models. Calculations are also needed to determine the system's sensitivity to the effects of shell thickness (e.g., Al-Shamali et al., 2004), the effects of stably-stratified regions (e.g., Zhang and Schubert, 2000; Stanley and Bloxham, 2004), compositional convection and other mechanisms for angular momentum homogenization.

5.3. Summary

Our numerical models of thermal convection support the hypothesis that zonal winds on Uranus and Neptune are driven by vigorous mixing. In our models, we find that high Ra^* convection mixes and homogenizes angular momentum in the spherical shell. This mixing process generates a strong retrograde zonal flow in the equatorial region and prograde flows in the polar regions, similar to the observed wind patterns on Uranus and Neptune.

The angular momentum homogenization hypothesis provides a number of predictions concerning zonal flow generation in Boussinesq fluid layers. First, in the $Ra^* \gtrsim 1$ regime the zonal flow Rossby numbers are independent of the Ekman and Rayleigh numbers. Second, the depth of convection, i.e., the radius ratio, determines both the strength of the zonal flows and the latitudinal width of the equatorial retrograde jet. Third, the zonal flows vary predominantly as a function of cylindrical radius, resulting in parabolic zonal flow profiles that are symmetric across the equatorial plane. This equatorial symmetry may lead to testable differences with shallow layer models and to detailed comparisons with velocity and thermal emission measurements of the ice giants.

While our convection models generate zonal flow patterns similar to the ice giants, they have yet to address certain aspects of the planetary observations. The amplitudes of the surface zonal flow Rossby numbers are almost an order of magnitude greater than those that exist on the ice giants. It is also uncertain whether or not the ice giants' internal heat fluxes are large enough to drive $Ra^* \gtrsim 1$ convection. However, our models suggest that vigorous mixing plays a fundamental role in the atmospheric dynamics on the ice giants and that these homogenization processes merit further investigation.

Acknowledgments

The authors wish to thank J. Friedson, E. King, P. Olson, A. Showman, K. Soderlund and two anonymous referees for helpful comments and suggestions. This work has been supported by funding from NASA's Planetary Atmospheres Grant NNG06GD12G (J.A.), NSERC Canada (M.H.) and DFG Germany (J.W.). Computational resources were provided by the Western Canada Research Grid (WestGrid).

References

Al-Shamali, F.M., Heimpel, M.H., Aurnou, J.M., 2004. Varying the spherical shell geometry in rotating thermal convection. Geophys. Astrophys. Fluid Dynam. 98, 153–169.

Allison, M., Del Genio, A.D., Zhou, W., 1994. Zero potential vorticity envelopes for the zonal-mean velocity of the Venus/Titan atmospheres. J. Atmos. Sci. 51, 694–702.

Atkinson, D.H., Pollack, J.B., Seiff, A., 1998. The Galileo probe Doppler wind experiment: Measurement of the deep zonal winds on Jupiter. J. Geophys. Res. 103, 22911–22928.

Aubert, J., Wicht, J., 2004. Axial and equatorial dipolar dynamo models with implications for planetary magnetic fields. Earth Planet Sci. Lett. 221, 409–419.

Aurnou, J.M., Heimpel, M.H., 2004. Zonal jets in rotating convection with mixed mechanical boundary conditions. Icarus 169, 492–498.

Aurnou, J.M., Olson, P.L., 2001. Strong zonal winds from thermal convection in a rotating spherical shell. Geophys. Res. Lett. 28, 2557–2559.

Aurnou, J.M., Andreadis, S., Zhu, L., Olson, P.L., 2003. Experiments on convection in Earth's core tangent cylinder. Earth Planet. Sci. Lett. 212, 119–134.

Beebe, R.F., 2005. Comparative study of the dynamics of the outer planets. Space Sci. Rev. 116, 137–154.

Bretherton, F.P., Turner, J.S., 1968. On the mixing of angular momentum in a stirred rotating fluid. J. Fluid Mech. 32, 449–464.

Brun, A.S., Toomre, J., 2002. Turbulent convection under the influence of strong rotation: Sustaining a strong differential rotation. Astrophys. J. 570, 865–885.

Busse, F.H., 1976. A simple model of convection in the jovian atmosphere. Icarus 20, 255–260.

Busse, F.H., 2002. Convective flows in rapidly rotating spheres and their dynamo action. Phys. Fluids 14, 1301–1314.

Cessi, P., 1998. Angular momentum and temperature homogenization in the symmetric circulation of the atmosphere. J. Atmos. Sci. 55, 1997–2015.

Cho, J.Y.K., Polvani, L.M., 1996. The morphogenesis of bands and zonal winds in the atmospheres on the giant outer planets. Science 273, 335–337.

Cho, J.Y.K., Menou, K., Hansen, B.M.S., Seager, S., 2003. The changing face of the extrasolar giant planet HD 209458b. Astrophys. J. 587, L117–L120.

Christensen, U.R., 2001. Zonal flow driven by deep convection on the major planets. Geophys. Res. Lett. 28, 2553–2556.

Christensen, U.R., 2002. Zonal flow driven by strongly supercritical convection in rotating spherical shells. J. Fluid Mech. 470, 115–133.

Christensen, U., Olson, P., Glatzmaier, G.A., 1999. Numerical modeling of the geodynamo: A systematic parameter study. Geophys. J. Int. 138, 393–409.

Christensen, U., and 15 colleagues, 2001. A numerical dynamo benchmark. Phys. Earth Planet. Int. 128, 25–34.

Evonuk, M., Glatzmaier, G.A., 2004. 2D studies of various approximations used for modeling convection in the giant planets. Geophys. Astrophys. Fluid Dynam. 98, 241–255.

Fry, P.M., Sromovsky, L., 2004. Keck 2 AO observations of Neptune in 2003 and 2004. Bull. Am. Astron. Soc. 36, 1103.

Gilman, P.A., 1977. Nonlinear dynamics of Boussinesq convection in a deep rotating spherical shell. I. Geophys. Astrophys. Fluid Dynam. 8, 93–135.

Gilman, P.A., 1978. Nonlinear dynamics of Boussinesq convection in a deep rotating spherical shell. II. Effects of temperature boundary conditions. Geophys. Astrophys. Fluid Dynam. 11, 157–179.

Glatzmaier, G.A., 1984. Numerical simulations of stellar convective dynamos. I. The model and the method. J. Comput. Phys. 55, 461–484.

Glatzmaier, G.A., Gilman, P.A., 1982. Compressible convection in a rotating spherical shell. V. Induced differential rotation and meridional circulation. Astrophys. J. 256, 316–330.

Gough, D.O., Lynden-Bell, D., 1968. Vorticity expulsion by turbulence: Astrophysical implications of an Alka–Seltzer experiment. J. Fluid Mech. 32, 437–447.

Guillot, T., 1999. Interiors of giant planets inside and outside the Solar System. Science 286, 72–77.

Guillot, T., 2005. The interiors of giant planets: Models and outstanding questions. Annu. Rev. Earth Planet. Sci. 33, 493–530.

Guillot, T., Stevenson, D.J., Hubbard, W., Saumon, D., 2004. The interior of Jupiter. In: Bagenal, F., Dowling, T.E., McKinnon, W.B. (Eds.), Jupiter: The Planet, Satellites and Magnetosphere. Cambridge Univ. Press, Cambridge.

Hammel, H.B., Rages, K., Lockwood, G.W., Karkoschka, E., de Pater, I., 2001. New measurements of the winds of Uranus. Icarus 153, 229–235.

Hammel, H.B., de Pater, I., Gibbard, S., Lockwood, G.W., Rages, K., 2005. Uranus in 2003: Zonal winds, banded structure, and discrete features. Icarus 175, 534–545.

Held, I.M., Hou, A.Y., 1980. Nonlinear axially symmetric circulations in a nearly inviscid atmosphere. J. Atmos. Sci. 37, 515–533.

Heimpel, M.H., Aurnou, J.M., 2007. Turbulent convection in rapidly rotating spherical shells: A model for equatorial and high-latitude jets on Jupiter and Saturn. Icarus 187, 540–557.

Heimpel, M.H., Aurnou, J.M., Wicht, J., 2005. Simulation of equatorial and high-latitude jets on Jupiter in a deep convection model. Nature 438, 193–196.

Holme, R., 1997. Three-dimensional kinematic dynamos with equatorial symmetry: Application to the magnetic fields of Uranus and Neptune. Phys. Earth Planet. Int. 102, 105–122.

Hopfinger, E.J., Browand, F.K., Gagne, Y., 1982. Turbulence and waves in a rotating tank. J. Fluid Mech. 125, 505–534.

Hubbard, W.B., Stevenson, D.J., 1984. Interior structure of Saturn. In: Gehrels, T., Matthews, M.S. (Eds.), Saturn. Univ. of Arizona Press, Tucson.

Hubbard, W.B., Nellis, W.J., Mitchell, A.C., Holmes, N.C., Limaye, S.S., McChandless, P.C., 1991. Interior structure of Neptune: Comparison with Uranus. Science 253, 648–651.

Hubbard, W.B., Podolak, M., Stevenson, D.J., 1995. The interior of Neptune. In: Cruikshank, D. (Ed.), Neptune and Triton. Univ. of Arizona Press, Tucson.

Ingersoll, A.P., 1990. Atmospheric dynamics of the outer planets. Science 248, 308–315.

Ingersoll, A.P., Pollard, D., 1982. Motion in the interiors and atmospheres of Jupiter and Saturn: Scale analysis, anelastic equations, barotropic stability criterion. Icarus 52, 62–80.

Kerswell, R.R., 2002. Elliptical instability. Annu. Rev. Fluid Mech. 34, 83–113.

Kirk, R.L., Stevenson, D.J., 1987. Hydromagnetic constraints on deep zonal flow in the giant planets. Astrophys. J. 316, 836–846.

Liu, Y., Ecke, R.E., 1997. Heat transport scaling in turbulent Rayleigh–Bénard convection: Effects of rotation and Prandtl number. Phys. Rev. Lett. 79, 2257–2260.

Lodders, K., Fegley Jr., B., 1998. The Planetary Scientist's Companion. Oxford Univ. Press, Oxford.

Marley, M.S., McKay, C.P., 1999. Thermal structure of Uranus' atmosphere. Icarus 138, 268–286.

Miesch, M.S., Elliott, J.R., Toomre, J., Clune, T.L., Glatzmaier, G.A., Gilman, P.A., 2000. Three-dimensional spherical simulations of solar convection. I. Differential rotation and pattern evolution achieved with laminar and turbulent states. Astrophys. J. 532, 593–615.

Nellis, W.J., Weir, S.T., Mitchell, A.C., 1996. Metallization and electrical conductivity of hydrogen in Jupiter. Science 273, 936–938.

Peltier, W.R., Stuhne, G.R., 2002. The upscale turbulent cascade: Shear layers, cyclones and gas giant bands. In: Pearce, R.P. (Ed.), Meteorology at the Millennium. Academic Press, London.

Perez-Hoyos, S., Sanchez-Lavega, A., French, R.G., Rojas, J.F., 2005. Saturn's cloud structure and temporal evolution from ten years of Hubble Space Telescope images (1994–2003). Icarus 176, 155–174.

Podolak, M., Hubbard, W.B., Stevenson, D.J., 1991. Models of Uranus' interior and magnetic field. In: Bergstralh, J.T., Miner, E.D., Matthews, M.S. (Eds.), Uranus. Univ. of Arizona Press, Tucson.

Porco, C.C., and 23 colleagues, 2003. Cassini imaging of Jupiter's atmosphere, satellites and rings. Science 299, 1541–1547.

Porco, C.C., and 34 colleagues, 2005. Cassini imaging science: Initial results on Saturn's atmosphere. Science 307, 1243–1247.

Rhines, P.B., 1975. Waves and turbulence on a beta-plane. J. Fluid Mech. 69, 417–443.

Russell, C.T., Yu, Z.J., Kivelson, M.G., 2001. The rotation period of Jupiter. Geophys. Res. Lett. 28, 1911–1912.

Ruzmaikin, A.A., Starchenko, S.V., 1991. On the origin of Uranus and Neptune's magnetic fields. Icarus 93, 82–87.

Sanchez-Lavega, A., Rojas, J.F., Sada, P.V., 2000. Saturn's zonal winds at cloud level. Icarus 147, 405–420.

Scorer, R.S., 1966. Origin of cylcones. Sci. J. 2, 46–52.

Semeniuk, K., Shepherd, T.G., 2001. The middle-atmosphere Hadley circulation and the equatorial inertial adjustment. J. Atmos. Sci. 58, 3077–3096.

Showman, A.P., Gierasch, P.J., Lian, Y., 2006. Deep zonal winds can result from shallow driving in a giant-planet atmosphere. Icarus 182, 513–526.

Smith, M.D., Gierasch, P.J., 1995. Convection in the outer planet atmospheres including *ortho–para*-hydrogen conversion. Icarus 116, 159–179.

Sromovsky, L.A., Limaye, S.S., Fry, P.M., 1993. Dynamics of Neptune's major cloud features. Icarus 105, 110–141.

Sromovsky, L.A., Fry, P.M., Dowling, T.E., Baines, K.H., Limaye, S.S., 2001. Neptune's atmospheric circulation and cloud morphology: Changes revealed by 1998 HST imaging. Icarus 150, 244–260.

Stanley, S., Bloxham, J., 2004. Convective-region geometry as the cause of Uranus' and Neptune's unusual magnetic fields. Nature 428, 151–153.

Sukoriansky, S., Galperin, B., Dikovskaya, N., 2002. Universal spectrum of two-dimensional turbulence on a rotating sphere and some basic features of atmospheric circulation on giant planets. Phys. Rev. Lett. 89, doi:10.1103/PhysRevLett.89.124501.

Suomi, V.E., Limaye, S.S., Johnson, D.R., 1991. High winds of Neptune: A possible mechanism. Science 251, 929–932.

Tilgner, A., Busse, F.H., 1997. Finite amplitude convection in rotating spherical fluid shells. J. Fluid Mech. 332, 359–376.

Tritton, D.J., 1987. Physical Fluid Dynamics. Oxford Univ. Press, Oxford.

Vasavada, A.R., Showman, A.P., 2005. Jovian atmospheric dynamics: An update after Galileo and Cassini. Rep. Prog. Phys. 68, 1935–1996.

Wicht, J., 2002. Inner-core conductivity in numerical dynamo simulations. Phys. Earth Planet. Int. 132, 281–302.

Williams, G.P., 2003. Jovian dynamics. Part III. Multiple, migrating, and equatorial jets. J. Atmos. Sci. 60, 1270–1296.

Yano, J.I., Talagrand, O., Drossart, P., 2005. Deep two-dimensional turbulence: An idealized model for atmospheric jets of the giant outer planets. Geophys. Astrophys. Fluid Dynam. 99, 137–150.

Zhang, C.Z., 1997. Uranus and Neptune interior models. Earth Moon Planets 75, 17–24.

Zhang, K., 1992. Spiraling columnar convection in rapidly rotating spherical fluid shells. J. Fluid Mech. 236, 535–554.

Zhang, K., Schubert, G., 2000. Teleconvection: Remotely driven thermal convection in rotating stratified spherical layers. Science 290, 1944–1947.

Zhang, X., Boyer, D.L., Fernando, H.J.S., 1997. Turbulence-induced rectified flows in rotating fluids. J. Fluid Mech. 350, 97–118.